Bank erosion processes measured with UAV-SfM along complex banklines of a straight mid-sized river reach

Gonzalo Duró[1], Alessandra Crosato[1,2], Maarten G. Kleinhans[3], Wim S. J. Uijttewaal[1]

[1] Department of Hydraulic Engineering, Delft University of Technology, PO Box 5048, 2600 GA Delft, the Netherlands
[2] Department of Water Engineering, IHE-Delft, PO Box 3015, 2601 DA Delft, the Netherlands
[3] Department of Physical Geography, Utrecht University, PO Box 80115, 3508 TC Utrecht, the Netherlands

Correspondence to: Gonzalo Duró (G.Duro@tudelft.nl)

We apply Structure from Motion (SfM) photogrammetry with imagery from an Unmanned Aerial Vehicle (UAV) to measure bank erosion processes along a mid-sized river reach. This technique offers a unique set of characteristics compared to previously used methods to monitor banks, such as high resolution and relatively fast deployment in the field. We analyse the retreat of a 1.2 km restored bank of the Meuse River which has complex vertical scarps laying on a straight reach, features that present specific challenges to the UAV-SfM application. We surveyed eight times within a year with a simple approach, combining different photograph perspectives and overlaps to identify an effective UAV flight. The accuracy of the Digital Surface Models (DSMs) was evaluated with RTK GPS points and an airborne laser scanning of the whole reach. An oblique perspective with eight photo overlaps and 20 m of cross-sectional ground-control point distribution was sufficient to achieve the relative precision to observation distance of ~1:1400 and 3 cm RMSE, complying with the required accuracy. A complementary nadiral view increased coverage behind bank toe vegetation. Sequential DSMs captured signatures of the erosion cycle such as mass failures, slump-block deposition, and bank undermining. Although UAV-SfM requires low water levels and banks without dense vegetation as many other techniques, it is a fast-in-the-field alternative to survey reach-scale riverbanks in sufficient resolution and accuracy to quantify bank retreat and identify morphological features of the bank failure and erosion processes. Improvements to the adopted approach are recommended to achieve higher accuracies.

Keywords: Riverbank erosion monitoring, erosion cycle, restoration, Unmanned Aerial Vehicles (UAV), Structure from Motion (SfM).

1 Introduction

Bank erosion is a fundamental process in morphologically active river systems, and much research has been devoted to understanding, quantifying and modelling it from disciplines such as engineering, geomorphology, geology and ecology. River bank erosion involves interconnected physical, chemical and biological processes (e.g., Hooke, 1979; ASCE, 1998; Rinaldi and Darby, 2008), resulting in a complex phenomenon that is difficult to thoroughly understand and predict (e.g.,

Siviglia and Crosato, 2016). Predicting and monitoring bank erosion is necessary for sound river management strategies and also important for both socio-economic problems, such as preventing material losses (e.g., Nardi et al., 2013), and environmental challenges, for instance, promoting habitat diversity through river restoration (e.g., Florsheim et al., 2008) and improving water quality (e.g., Reneau et al., 2004).

5   Bank erosion can be monitored with different spatial resolutions, time frequencies and accuracies. The techniques that identify the temporal change in vertical bank profiles detect and quantify the different phases of the erosion cycle (Thorne and Tovey, 1981). This characteristic helps distinguishing the factors influencing bank erosion and their relative role in the whole process (e.g., Henshaw et al., 2013). On the other hand, a simple record of sequential mass failure events (see Fukuoka, 1994, for a graph of failure-driven retreat) is sufficient to track rates of local bankline retreat and estimate eroded

10   volumes, but does not provide further information on the role of single factors governing the bank erosion process. In navigable rivers, for instance, it is important to differentiate the effects of vessel-induced waves from the effects of river flow, as well as those of high flows and water level fluctuations. This requires high spatial resolution and relatively frequent measurements that usually involve expensive equipment and field logistics when monitoring large extensions. In this context, Structure from Motion (SfM) photogrammetry appears a promising easy-to-use technique to measure bank erosion

15   processes along extensive distances (Fonstad et al., 2013).

We apply SfM with imagery from a low-cost multi-rotor Unmanned Aerial Vehicle (UAV) to measure horizontal and vertical bank alignments at the process scale along a mid-sized river reach with a standard workflow. In order to do that, we compare the SfM-based Digital Surface Model (DSM) with Real-Time Kinematic (RTK) GPS measurements and Airborne Laser Scanning (ALS), and analyse erosion features in bank profiles. We consider the erosion cycle as a reference

20   to distinguish approaches that measure bank erosion in qualitative terms, and we define a minimum required resolution and accuracy of 1/25 times the bank height, for quantitative analysis. The case study is a 1.2 km straight river reach with complex vertical scarps. This type of linear domain with vertical surfaces represent challenges to the UAV-SfM application, since special UAV paths and camera angles may be needed to capture the bank area and rather aligned GCPs along banks may result in rotated solutions during the model linear transformation.

25   This work first introduces the characteristic erosion cycle of banks and a summary of available techniques to measure them. Then, we describe the adopted approach to apply UAV-SfM to measure bank erosion. Afterwards, we show the precision of the digital surface models relative to other techniques, an analysis of the particular errors that may arise from the use of UAV-SfM to survey long riverbanks, and the features and processes identifiable from the bank profiles. Later, we discuss the precision and error sources of UAV-SfM with the adopted approach, the differences found between two reach-

30   scale techniques, and the particular challenges and recommendations to apply UAV-SfM for bank erosion. Finally, we discuss advantages and limitations of UAV-SfM compared to other available methods to measure bank erosion processes.

2 Framework of analysis

2.1 Bank erosion cycle

Bank erosion may consist of three phases (Thorne and Tovey, 1981): fluvial entrainment of near-bank river-bed and bank material, mass failure, and disintegration and removal of slump blocks. These three phases are particularly important for

5   cohesive banks since their retreat is typically delayed by the protection offered by slump blocks at their toe (Thorne, 1982; Lawler, 1992; Parker et al., 2011). The waste material settles at the bank toe where it remains for a time depending on its resistance to fluvial erosion and on the available capacity to transport the blocks. In contrast, loose waste material from non-cohesive banks is generally transported away relatively quicker by the river flow, leaving the bank sooner unprotected. Entrainment of near-bank bed material and the intact bank face occurs once the bank toe is exposed again (e.g., see Clark

10   and Wynn, 2007), which continues until the collapse of the upper bank. Mass failure occurs due to geotechnical instability, which can be triggered by different factors, such as fluvial bank-toe erosion (e.g., Darby et al., 2007) or a rapid drawdown of the river stage (e.g., Thorne and Tovey, 1981; Rinaldi et al., 2004).

Not only the river flow triggers the bank erosion cycle but other drivers can contribute to it as well. For instance, subaerial processes may weaken the bank and accelerate later fluvial erosion (Lawler, 1992; Kimiaghalam et al., 2015) or

15   also act as direct agent of erosion (Couper and Maddock, 2001). These effects are included in the entrainment phase for the former example and in the mass failure phase for the latter, which respectively promote entrainment or deliver material to the bank toe. Figure 1 illustrates the three phases of erosion in schematic cohesive banks. This representation shows a homogeneous soil which undergoes a continuous cycle of erosion with varying water levels.
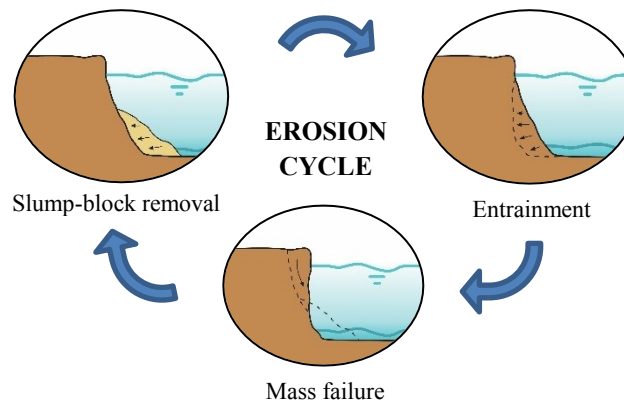
Figure 1: Schematic bank erosion phases: Slump-block removal (left), entrainment of bare bank (right) and incipient mass failure (centre)

Bank erosion can be analysed and measured at two different scales, i.e., the fluvial process and the river cross

25   section. The measurement at the process scale considers the bank face disintegration over time with evidence of erosion phases (Fig. 1): the mechanisms of erosion develop and are captured at the vertical dimension of the bank. The measurement of bank erosion at the cross-sectional scale, which can be referred to as bankline retreat, consists of tracking banklines over

time. In this case, the focus is on the planimetric changes of the bank edge and estimations of eroded volumes and sediment yield. The former approach deals with processes and mechanisms (e.g., Rinaldi and Darby, 2008), whereas the latter with landscape development at larger spatial and temporal scales. Bank-erosion studies determine the survey method based on their aims and scales of interest, whereas in turn a given methodology constraints the scope of the findings (Massey, 2001; Couper, 2004). Thus, it is important to identify capabilities and limitations of each survey technique in the context of river banks, which are inherently steep features with small-scale irregularities independent of the scale of the river.

2.2 Techniques to measure bank erosion at different scales

Measuring techniques have four essential characteristics: the extent, resolution, quality and frequency of measurements. Extent refers to the area or distance along the river covered by each survey; resolution indicates the distance between surveyed points; quality is the precision of position of each surveyed point; and frequency derives from the time interval between consecutive surveys of the same spatial extent or point. The scale of interest may vary among disciplines (e.g., geomorphology, engineering, ecology), so that a diversity of techniques is available with varying spatio-temporal windows of inquiry (Lawler, 1993). Even though the methods currently adopted to measure river bank erosion range from photo-electric erosion pins to terrestrial laser scanning, they only have high resolution in either time or space (Couper, 2004; Rinaldi and Darby, 2008).

The methods to determine bankline retreat and to estimate eroded volumes are typical of remote sensing, for instance, ALS and aerial photography. The former technique has typical resolutions of 1 and 0.5 metres, and covers up to hundreds of square kilometres per day. Bailly et al., (2012) indicate decimetre vertical precision, which depends on several factors including beam footprint size, aircraft inertial measuring system, on-board GPS, vegetation cover and filtering technique. ALS has been successfully applied to identify river morphological features, such as bar tops (Charlton et al., 2003) and riffle–pool and step–pool sequences (Cavalli et al., 2008; Bailly et al., 2012). In addition, sequential ALSs were used to quantify volumes of eroded banks to subsequently estimate pollutant loads, achieving reasonable results for those aims (Thoma et al., 2005). However, banks are particularly steep areas where this technique tends to increase the elevation uncertainty (Bangen et al., 2014). Therefore banks are regions where lower ALS accuracies are expected compared to horizontal and flat areas.

Bank retreat can be estimated through approaches such as those described by Lawler (1993) that include planimetric resurveys for intermediate timescales (years) and sedimentological and botanical evidence for long timescales (centuries to millennia). Aerial photography interpretation has also been applied to measure bank migration, which is a useful source of information, especially if historical imagery is available over extended periods of time. Nevertheless, it provides only limited information on bank heights, for which this planform survey technique requires other methods to estimate eroded volumes. For example, photogrammetry can complementary serve to quantify volumetric changes from overlapping photographs (Lane et al., 2010); or ALS to provide recent topographic elevations and reconstruct past morphologies (Rhoades et al., 2009).

Measuring bank erosion at the process scale involves measuring the evolution of the vertical bank profile over time and several other techniques are currently available to that end. Traditional methods include erosion pins and repeated cross-profiling, which provide two-dimensional information with resolutions that respectively depend on the number of pins and points across the profile (Lawler, 1993). Erosion pins are simple and effective, but their accuracy may be affected by several factors, such as subaerial processes (Couper et al., 2002). More advanced versions are the photo-electric erosion pins that automatically track the bank face during different erosion phases (Lawler, 2005). Cross-profiling can be done with GPS or total stations with point accuracies of a few centimetres or millimetres, yet with spatial and temporal resolutions that may not be sensitive to very localized or intermittent erosion (e.g., Brasington et al., 2000).

Bank geometries can currently be surveyed at the process scale with their three-dimensional complexity through a number of techniques, whose geomorphic applications are broader than bank erosion studies: terrestrial photogrammetry, Terrestrial Laser Scanning (TLS), boat-based laser scanning and SfM photogrammetry. Terrestrial photogrammetry has shown detailed bank representations, with approximate resolutions of 2 cm and precision within 3 cm, covering up to 60 metres of banks (Barker et al., 1997; Pyle et al., 1997). All the same time, this method can be labour-intensive and requires an accessible bank (Bird et al., 2010), known camera positions and sensor characteristics, ground-control points, among other considerations (Lane, 2000). TLS has shown detailed erosion patterns from sequential surveys, with millimetre resolutions, which in practice are usually reduced to 2–5 centimetres, and approximate final accuracies of 2 cm (Resop and Hession, 2010; Leyland et al., 2015). O'Neal and Pizzuto (2011) proved the advantages of 3D TLS in capturing patterns (e.g., overhanging blocks) and quantifying eroded volumes over 2D cross-profiling. Even though TLS could cover thousands of meters, in practice the extents are generally smaller due to accuracy decrease, large incidence angles, occlusion, etc. (Telling et al., 2017), so several scans are necessary to measure long distances. For instance, Brasington et al. (2012) surveyed a 1 km river reach scanning every 200 m along the channel. An alternative boat-based laser scanning can continually survey banks with comparable resolutions and accuracies to those of TLS, with great time reduction but involving other field logistics, resources and post-processing (Alho et al., 2009).

2.2.1 Structure from Motion photogrammetry

Bangen et al., (2014) matched the resolution and practical extent of SfM photogrammetry to those of TLS, when SfM photogrammetry is used to survey river topography through aerial platforms (e.g., Fonstad et al., 2013). From terrestrial platforms, this technique has been applied to measure banks to show its potential use as survey technique with different sensors and processing systems (Micheletti et al., 2015; Prosdocimi et al., 2015). Micheletti et al. (2015) indicated root mean square errors (RMSE) within 7 cm, when combining a 5MP smartphone or a 16MP reflex camera with either PhotoModeler or 123D Catch processing systems. Prosdocimi et al. (2015) identified eroded areas of a collapsed riverbank and computed eroded and deposited volumes with a precision comparable to that of TLS.

The relatively recent and fast development of UAV technology to take airborne photographs has greatly expanded the applications of SfM photogrammetry (Eltner et al., 2016). Recently, SfM has been applied to quantify bank retreat at

streams and small rivers with a fixed-wing UAV along several kilometres with 12 cm resolution (Hamshaw et al., 2017). This study showed the UAV-SfM capabilities to produce extensive 2.5D DSM from a 100 m high nadiral view, which achieved 0.11 m mean error and 0.33 m RMSE compared to TLS. However, this work generated DSMs similar to those of ALS, which allow for volume computations and bankline retreat, but did not use the full 3D capacities to investigate

5   undermined banks or identify erosion processes.

        Applications of this combined technology span in scale and complexity, covering glacial dynamics (Immerzeel et al., 2014), landslides (Turner et al., 2015), agricultural watersheds (Ouédraogo et al., 2014), fluvial topography (Woodget et al., 2015), etc. The precision achieved relative to the camera-object distance for the mentioned diverse settings was approximately 1:1000, with distances ranging from 26 to 300 m and different cameras, lighting conditions and surface types.

10   Interestingly, this precision was also found for terrestrial SfM photogrammetry at different scales by James and Robson (2012). Other experiences showed lower accuracies, e.g., ~1:200 for moraine-mound topography (Tonkin et al., 2014), and on the other hand higher ones, such as ~1:2100 for fluvial changes after a flood event (Tamminga et al., 2015). Although it is not possible to generalize a precision for all settings, ~1:1000 seems an encouraging reference (RMSE of 10 cm for 100 m camera-object distance) to consider for unexplored conditions.

15   Several factors affect the precision of DSM obtained from UAV-SfM, such as surface textures at the field site (Cook, 2017), lighting conditions (Gómez-Gutierrez et al., 2014b), camera characteristics (Prosdocimi et al., 2015), GCP characteristics (Harwin and Lucieer, 2012), SfM algorithms (Eltner and Schneider, 2015), and photo overlaps, resolutions and perspectives (James and Robson, 2012; Micheletti et al., 2014). Knowledge to improve the quality of SfM digital surface models keeps expanding by investigating isolated variables, for example, assessing the influences of number and distribution

20   of GCPs (Clapuyt et al., 2016; James et al., 2017) or optimizing camera calibration procedures to manage without GCPs (Carbonneau and Dietrich, 2017). The flexibility, range, high resolution and accuracy that UAV-SfM proved in other conditions shows promising for analysing bank erosion processes throughout the scale of a mid-sized river.

        The monitoring of bank erosion processes in the case study herein has two specific challenges for the UAV-SfM technique. First, the bank has steep, vertical and undermined surfaces along the domain. Second, the target area is a straight

25   reach with a large length-to-width ratio. The first aspect may require non-conventional UAV paths and camera angles to be able to adequately capture the bank area. The second matter introduces a challenge to georeference the model with rather aligned GCPs, which may result in false solutions rotated around the GCP axis during the model linear transformation. This could be the case since GCPs are to be placed in the bank surroundings to be captured from the UAV, and this target area consist of an overall linear domain. Therefore, the GCP distribution and the image network geometry particularly have key

30   roles in the UAV-SfM workflow applied to measure bank erosion at the process scale.

3 Methodology

We used a flexible multi-rotor UAV platform to capture photographs from different perspectives of a 1200 m long riverbank and through SfM photogrammetry derived several DSMs over one year period. We describe the study location in Sect. 3.1, the UAV paths for photo acquisition in Sect. 3.2, and the SfM imagery processing in Sect. 3.3. In order to assess the capabilities of this survey technique with the adopted approach to measure bank erosion at the process scale we proceeded in four steps. First, we verified the elevation precision against 129 RTK GPS points of several DSMs obtained with diverse number of photographs and camera orientations. In this way, we identified an effective number of images to acquire the bank topography with high accuracy. Second, we compared the chosen DSM with airborne LIDAR points to analyse elevation precision over the whole river reach, differentiating between areas of bare ground, grassland and banks. Third, we verified the georeferentiation accuracy regarding the model rotation around GCP axis. Fourth, we searched for bank features in SfM-based profiles and analogous ones from ALS, and for signatures of erosion processes along sequential SfM surveys. All data used herein is publicly accessible (Duró et al., 2018).

For the first step, the analysis of the minimum number of photographs needed to achieve the highest DSM accuracy, we compared the DSMs with RTK GPS measurements to quantify vertical precision. We took 129 points across eight profiles on 18-01-2017 (see Fig. 4) with a Leica GS14 RTK GPS, whose root mean square precisions according to the manufacturer specifications are 8 mm + 0.5 ppm in horizontal and 15 mm + 0.5 ppm in vertical directions. On the same date, we flew the UAV along the bank four times with different camera angles and perspectives. Eight photograph combinations were considered to derive 8 DSMs. Then, the comparisons were done with the elevation differences between the GPS points and the corresponding closest ones of the DSM point clouds (e.g., Westoby et al, 2012; Micheletti et al., 2015). We used CloudCompare software (Girardeau-Montaut, 2017) for these computations.

In the second step, we compared the selected DSM from the previous analysis with ALS, to analyse topographic differences over the whole river reach. The ALS data was acquired on 17-01-2017 from an airplane at 300 meters above the ground level. The laser scanner, a *Riegl LMS-Q680i,* measured a minimum of 10 points per square metre with an effective pulse rate of 266 kHz. We did not have access to the raw data and used the automatically generated 0.5 m grid. We tested the ALS elevation precision against the 129 RTK GPS points using the vertical component of the closest distance to a local Delaunay triangulation of the ALS grid, due to the different resolutions between both datasets. Then, we computed the distances between the ALS grid points and the corresponding nearest ones of the DSM point cloud. We did both computations with the standard cloud/cloud distance tool of CloudCompare, distinguishing between surfaces of grassland, bare ground and bank.

Third, we analysed the DSM spatial stability with respect to the potential axis of rotation around the GCPs. The GCPs distributed over the floodplain along the near-bank area defined the linear transformation from an arbitrarily scaled coordinate system to the real-world coordinates. In order to verify that the DSM was stable and the tendency to rotate around co-linear solutions did not affect the accuracy beyond the survey target, we computed a regression line with the GCPs to

identify the potential axis of rotation for the DSM domain. Then, we projected the DSM elevation errors corresponding to the GPS points onto the plane perpendicular to the regression line. Afterwards, we computed a second regression line with those points to evaluate the alignment of errors across the potential axis of rotation.

Fourth, we made profiles across six sections of dissimilar erosion rates to contrast the bank representations of i) the SfM DSM, ii) the triangulated ALS grid, and iii) the RTK GPS points. The profiles were extracted with MATLAB using i) the Geometry Processing Toolbox (Jacobson et al., 2017) adapted to slice triangle meshes, ii) a linear interpolation across the triangulated ALS grid, and iii) a projection of the RTK GPS points onto the exact cross-section locations. Then, we identified and analysed a cross section over which sequential SfM-UAV surveys showed different stages of the erosion cycle, since the bank erosion cycle was used as a reference to distinguish between techniques capable of measuring at either the process or the cross-sectional scale.

3.1 Study site

The study site is a restored reach of the Meuse River, which used to be a single-thread freely meandering river. The river was canalized to a straight reach of 120 m width, the banks were protected and the water levels regulated to improve navigability. However, several kilometres of banks have been recently restored through the removal of revetments and groynes, following the EU Water Framework Directive 2000/60/EC (http://data.europa.eu/eli/dir/2000/60/oj). This reactivated erosion processes to improve the natural value of the river. Important questions have then arisen regarding bank retreat rates and the new equilibrium of the river width. Monitoring bank evolution is necessary to answer these questions and to identify the need, if so, to intervene and at which locations.

The study site is the left bank of a 1200 m long straight reach (Fig. 2) located between the Sambeek and Grave weirs in southeast Netherlands. Seven years after restoration, this reach presents different bank retreat patterns, with sub-reaches of rather uniform erosion and others with embayments of different lengths. Grassy fields used for grazing cover the riparian zone, followed by crop fields across the floodplain. In the near-bank area there are poplar trees every 100 m, some of which have been dislodged during the erosion progression, which is possible to appreciate in Fig. 2 (left) considering the ~200 m embayment between the foreground tree and the next in the background.

Figure 2: Restored bank in the Meuse River, upstream view of first 300 m (left) and downstream view of middle 500 m (right). Bank erosion has caused a series of bays in the 1,200 meter restored reach. Note eroded bank sediment in suspension.

The study site was surveyed eight times with the UAV in 2017. An extraordinary low water level in January provided the opportunity to compare the SfM photogrammetry with ALS and RTK GPS not only for the banks and floodplain, but also for the sub-aqueous terrace at the bank toe (see schematic cross sections in Fig. 2). This terrace was composed of bare soil, without vegetation or obstructions, which adds an extra surface for the comparative analysis. This extraordinary exposure was the consequence of a ship accident against the downstream weir of Grave (on 30 December 2016).

3.2 UAV flights for image acquisition

We used the consumer-grade UAV DJI Phantom 4 to take images of the banks. It has a built-in camera with a 1/2.3" 12 megapixels sensor and a 94° horizontal angle of view. Prior to the image acquisition, a network of Ground-Control Points (GCPs) was distributed on the floodplain to georeference the DSMs (see Fig. 4). The GCP were spaced every approximately 50 metres along the reach, roughly following the tortuous bankline and avoiding proximity to trees, to simplify the field work and facilitate the GCP visibility from the UAV paths (see Fig. 3-4). This approach did not include GCP locations at different elevations, as for instance at the bank toe, and relied on the cross-sectional GCP distribution for the stability of the DSM georeferentiation (see Sect. 3.3). The GCPs were 40 by 40 cm black ceramic tiles (Fig. 3c) fixed to the ground with a circular reflector (12 cm CD) at its centre for their fast recognition in the photographs (Fig. 3d-e show how a GCP is seen from tracks 1 and 2). We measured the GCP coordinates using the Leica GS14 RTK GPS unit, which was also deployed for the cross-profiling.

An initial flight plan was designed using UgCS software to photograph the banks from four different perspectives, to later compare the results of diverse combinations and find a convenient photo set to survey the target topography in subsequent campaigns. The UAV flew four times in straight parallel lines along the banks (Fig. 3a,b,f) to simplify the set-up and save flying time, compared to paths that follow changes in bankline or include paths across the domain. The first track took oblique photos from above the river at a height of 25 metres and an average (oblique) distance to the bank of 40 metres (~25 m from the least retreated bankline). The second track had a top view from 40 metres above the floodplain level along the tree line (Fig. 2–4). The third and fourth tracks followed the same path as the second one in respective upstream and downstream directions, but the camera angle was 50 degrees forward inclined from the horizontal plane (see photo footprints in Fig. 4). These perspectives were thought to capture the tortuous and complex bank surface (Fig. 2, 3a and 4), including undermined upstream- and downstream-facing scarps, with an average ground resolution of 2.1 cm per pixel. We considered a minimum resolution and accuracy of 1/25 times the bank height of the river as a requirement to detect erosion processes, which resulted in a maximum acceptable precision of 14 cm for the maximum bank height of 3.5 m at the case study.

We tested five specific combinations of photographs from the different UAV tracks. *Test 1* corresponds to the photo set of the first track only, which has the side view with the optimal coverage of the bank. *Test 2* stands for the nadir view

alone, which is similar to the viewpoint of classic aerial photography. *Test 3* is a combination of the previous two sets. *Test 4* combines tracks 3 and 4, i.e. both paths from above the bank with the oblique forward perspectives in upstream and downstream direction, which allows views on all parts of the irregular banks. Finally, *test 5* utilizes the four tracks with all photographs (Table 1).

5   We also used the first oblique track to evaluate the minimum longitudinal photo overlap to efficiently capture the bank relief. The photo overlap along the river is a function of the UAV speed and distance to the bank, for a given maximum photo sampling frequency, which in the case of the deployed UAV is one every 2 seconds. Then, flying at 2 m/s along track 1 resulted in 20 photo overlaps for the most retreated areas and 16 for those zones with least bank retreat, which corresponds to 95% and 93.7% image overlap, respectively. Afterwards in the processing phase, we successively selected a
10   decreasing number of overlaps by twos that resulted in four DSMs. These were *test 1a* when using all photos from track 1 (which is the same set as the aforementioned test 1), *test 1b* when using half of them, and so forth for *test 1c* and *test 1d* (see Table 1).

Table 1. Number of photographs and overlaps for the tests

	Test 1a	Test 1b	Test 1c	Test 1d	Test 2	Test 3	Test 4	Test 5
Track 1	293	147	73	37		147		293
Track 2					232	232		232
Track 3							232	232
Track 4							232	232
Min. overlaps	16	8	4	2	7	15	26	49
Max. overlaps	20	10	5	2	7	17	26	53

15   **3.3 SfM workflow**

The principles of SfM photogrammetry are similar to those of digital photogrammetry, but camera positions and lens characteristics are not specified in the former to reconstruct 3D structures. The camera extrinsic and intrinsic parameters are automatically estimated via tracking and matching pre-defined features in overlapping photos and an iterative bundle adjustment procedure, which results in a sparse point cloud (Hartley and Zisserman, 2003; Snavely et al., 2008; Westoby et
20   al., 2012). Afterwards, the (dense) point matching is done at pixel scale to generate a detailed point cloud of the scene that has the final survey resolution.

       GCPs are commonly used to reference the model to a geographical coordinate system, to compute erosion rates and processes through sequential surveys. The georeferencing process involves the Helmert transformation of the point cloud through 7 parameters that adjust its scale, position and rotation in a linear and rigid way (Fonstad et al., 2013). The
25   estimation of these parameters is done through a least-squares regression with the GCPs identified in the UAV images. The propagation of linear errors is thus given by the accuracy with which the GCPs were measured (in this study with the RTK

GPS) and then identified in the photographs. Further in the workflow, GCPs can be used to refine the camera parameters estimated during the bundle adjustment, to reduce the non-linear errors that the estimation of the camera parameters may induce (Carbonneau et al., 2017). Ideally, well distributed, precisely measured, and accurately identified GCPs avoid excessive linear and non-linear errors in the point cloud. Yet, a third type of error given by the automated image matching process cannot be prevented with GCPs. These are local and random errors and represent the classic concept of precision.

We used Agisoft PhotoScan software to process the imagery. The camera yaw, pitch and roll recorded during the UAV flight from different perspectives (Table 1) were input to ensure that the image matching assigned all photos into a single model (Stöcker et al., 2015). For this step we used three GCPs along the reach, two at the extremes and one at the middle, all close to the bank and easily visible from tracks 1 and 2. These approximate orientations and a priori known ground points helped obtaining a consistent sparse point cloud of the bank along the entire reach. The resulting camera positions and orientations of the photo alignment are visible in Fig. 3a, evidencing the UAV tracks. This figure also shows the DSM textured with colours from the photographs, in which the green area on the left side with white patches corresponds to the floodplain partially covered with snow (see also Fig. 3d-f) and the right brownish area is the terrace at the bank toe, with snow remains as well.
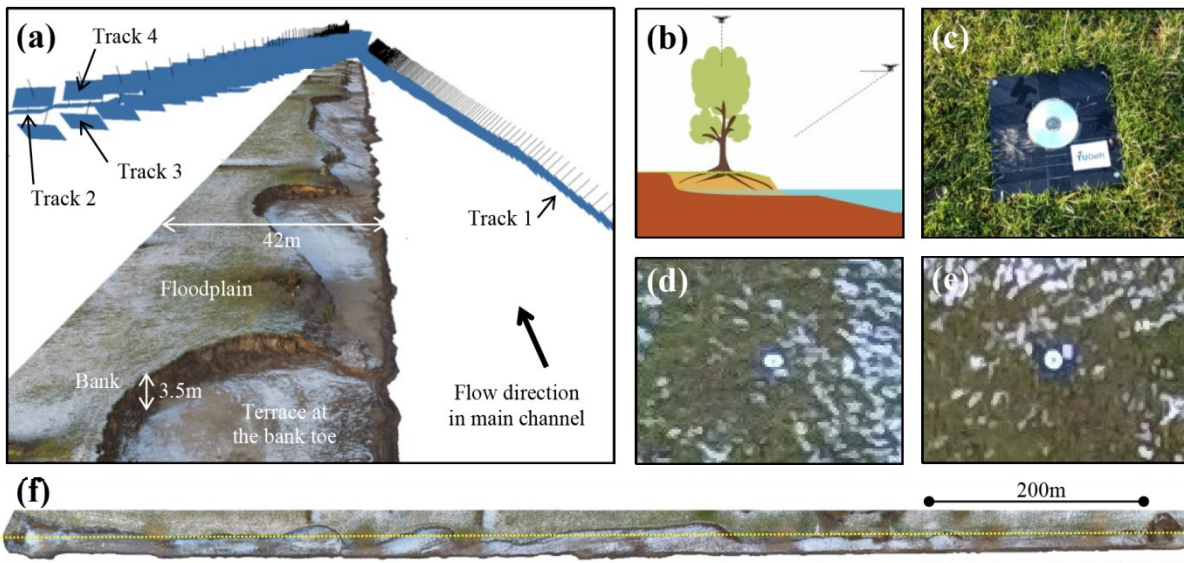
Figure 3: a) Camera positions and orientations in perspective view. The digital surface model shows the low-water condition during January 2017, which exposed a terrace at the bank toe. b) Cross-sectional scheme of UAV paths. c) Ceramic plaque with CD as ground-control point on the floodplain. d) GCP in photograph from track 1. e) Same GCP from track 2. f) Top view of DSM with UAV track 1 in blue and tracks 2-4 in yellow.

After obtaining the sparse point cloud, we identified the remaining 15 GCPs (Fig. 4) in the photographs, helped by their estimated locations in the model. Then, we refined the camera parameters by minimizing the sum of GCP reprojection and misalignment errors, i.e., using the camera optimization option in PhotoScan. This adjusts the estimated point cloud by reducing non-linear deformations. Once the dense point cloud was computed, we removed the points outside the area of

interest, as well as those points at the water surface, tree canopies and individual bushes at the floodplain. Finally, the point cloud was triangulated and interpolated to generate a TIN, through the *arbitrary* surface option and the highest number of mesh faces suggested in PhotoScan. This mesh consisted of a non-monotonic surface that was later processed in MATLAB to plot 2D cross sections.
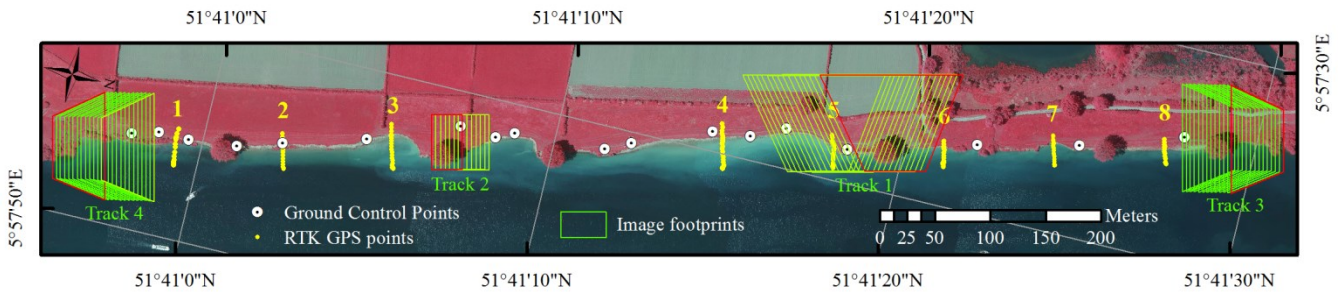
Figure 4: Study reach of the Meuse River with GCPs, RTK GPS measurements with cross-section locations and numbers, and some image footprints for all UAV tracks.

4 Results

4.1 DSM precision: identifying necessary photographs

The sequentially decreasing photo overlaps of Track 1 (Table 1) produced four DSMs, tests *1a–1d*, whose elevation differences with the 129 RTK GPS points are presented in the histograms of Fig. 5. The elevation errors mostly ranged within 10 cm in all tests, but the mean and standard deviation (SD) presented some differences (Table 2 and dot with bar in Fig. 5). Tests *1a*, *1b* and *1c* presented mean values smaller than 1 cm and SD within 3–4 cm, while for test *1d* these values increased to 4 cm and 7 cm respectively (Table 2, rows 1–2). The mean errors on the bank area alone for test *1a*, *1b* and *1c* were lower than 1 cm (Table 2, row 5), but test *1c* had a higher SD of 7 cm compared to 4 and 3 cm of tests *1a* and *1b* respectively (Table 2, row 6). Then, tests *1a* and *1b* had the highest precisions and showed little error differences between them: less than 1 cm for all values in Table 2. Consequently, test *1b* with eight photo overlaps was as effective as test *1a* with 16 overlaps to achieve the highest DSM accuracy. In addition, test *1b* fully covered the tortuous bank area in contrast to test *1c*, especially at the perpendicular stretches of embayments (Fig. 3–4), which assured the choice of 8 image overlaps over 4, despite the general close performance of the latter in terms of accuracy (Table 2, all rows). Therefore, test *1b* became the reference for tests *1* and was used in combination with test *2* to generate test *3*.
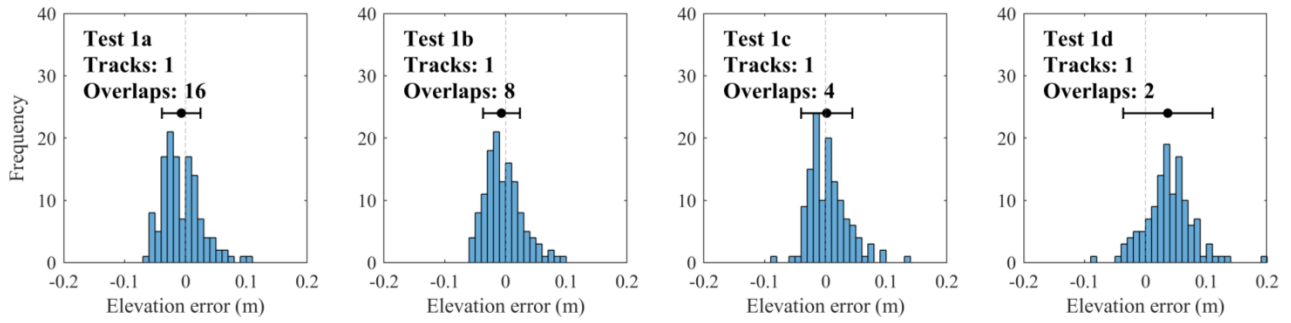
Figure 5: Elevation error distributions for SfM tests *1a*, *1b*, *1c*, and *1d*, assuming that the RTK points are correct and without error. Indicated overlaps are the minimum.

Table 2. Mean and standard deviation of elevation differences between SfM DSMs and GPS points. Colour intensity indicates the deviation from zero value with minimum/maximum of ±0.13 m.

Surface	Error (m)	Test 1a	Test 1b	Test 1c	Test 1d	Test 2	Test 3	Test 4	Test 5
All grounds	Mean	-0.01	0.00	0.00	0.04	0.03	-0.01	-0.05	0.00
	Std. dev.	0.03	0.03	0.04	0.07	0.03	0.03	0.05	0.03
Grassland	Mean	0.02	0.01	0.01	0.02	0.02	0.01	0.01	0.02
	Std. dev.	0.03	0.03	0.04	0.04	0.03	0.02	0.02	0.02
Bank	Mean	0.00	0.01	-0.01	-0.01	0.05	0.01	-0.03	0.01
	Std. dev.	0.04	0.03	0.07	0.13	0.03	0.03	0.04	0.03
Terrace	Mean	-0.02	-0.02	0.00	0.06	0.03	-0.02	-0.09	-0.01
	Std. dev.	0.02	0.03	0.03	0.06	0.03	0.02	0.03	0.02

Figure 6 shows the error distributions of the remaining four DSMs, i.e. tests *2–5*, which also were mostly within 10 cm, except for Test *4*. This test had evident higher errors than the rest, mostly concentrated at the terrace (Table 2, row 7). Tests *3* and *5* had the lowest mean elevation errors, both lower than 1 cm, with the same SD at all surfaces that were lower than 3 cm. Test *2* presented a similar SD, but the mean was biased 3 cm. This test in combination with test *1b* slightly reduced the SD errors of the latter (Table 2, rows 7 and 6), but without significant overall improvements. All in all, tests *1b*, *3* and *5* had the best performances with average errors lower than 1 cm and standard deviations within 3 cm, however with increasing number of photographs (Table 1). The most efficient one was then test *1b* that used the lowest number of photographs to achieve similar precision, especially on banks.
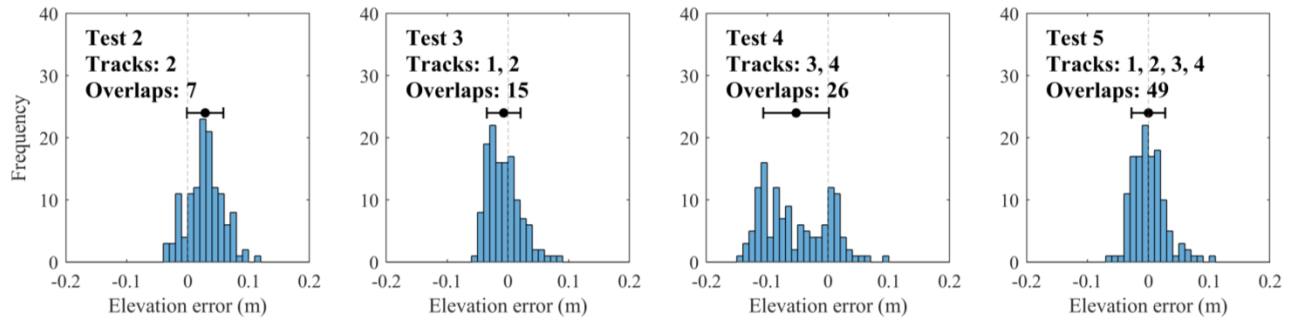
Figure 6: Elevation error distribution for tests 2, 3, 4, and 5. Ordinates indicate number of GPS points in each bin.

Interestingly, if we consider all tests, the elevation errors on grassland were similar to each other (Table 2, rows 3 and 6), means between 1 and 2 cm and SD between 2 and 4 cm, whereas the bank and terrace did not present this behaviour. Furthermore, while the bank values (Table 2, rows 4 and 7) did not correlate with those of all grounds (Table 2, rows 1–2), the terrace mean elevation differences (Table 2, row 5) linearly correlated with those of all grounds (Table 2, row 1) with R^2 = 0.97. Therefore, the error biases for all grounds throughout the tests were most likely due to the biases from the points over the terrace.

To conclude, despite virtually doubling the number of images in comparison with test 1b, the test *3* setup with a nadir track and a side-looking track was chosen for subsequent UAV surveys on the basis of two findings. First and most important, growing vegetation at the bank toe occluded parts of the target surface from the oblique camera perspective. Second, the GCPs on the floodplain laid almost horizontal, which made them easier to identify from the top-view during an initial phase of GCP recognition in the photographs. Moreover, we found at later surveys that growing grass on the floodplain was sometimes blocking GCP plaques from the angle of vision of UAV track 1, for which using the nadir view of track 2 was advantageous to locate the plaque centres, preventing the otherwise disuse of some GCPs.

4.2 DSM precision over the reach: comparison with ALS

Compared to the ALS grid, test *3* point cloud showed a good agreement over most of the reach. This is observable from Fig. 7a, corresponding to the blue areas that indicate elevation differences lower than 5 cm. However, two notable regions surpassed this difference: the bank and the extremes of the reach. The latter were zones beyond the GCPs, where higher errors in the DSM are expected when using parallel image directions due to inaccurate correction of radial lens distortion (James and Robson, 2014; Smith et al., 2014). Consequently, the results outside the GCP limits were not considered as reliable as those within, where distortion is minimal, and thus were discarded for the subsequent statistical comparisons (beyond the dashed lines in Fig. 7). Within the GCP bounds, the bank area presented relatively high elevation differences, which makes the bankline visible in Fig. 7. Moreover, another sloped area at end of the terrace also presented higher differences than surrounding areas, which is visible as a thin light-blue line at bottom of the domain in Fig. 7a (see also Fig. 3a-b for other perspectives of this slope toward the channel bed).
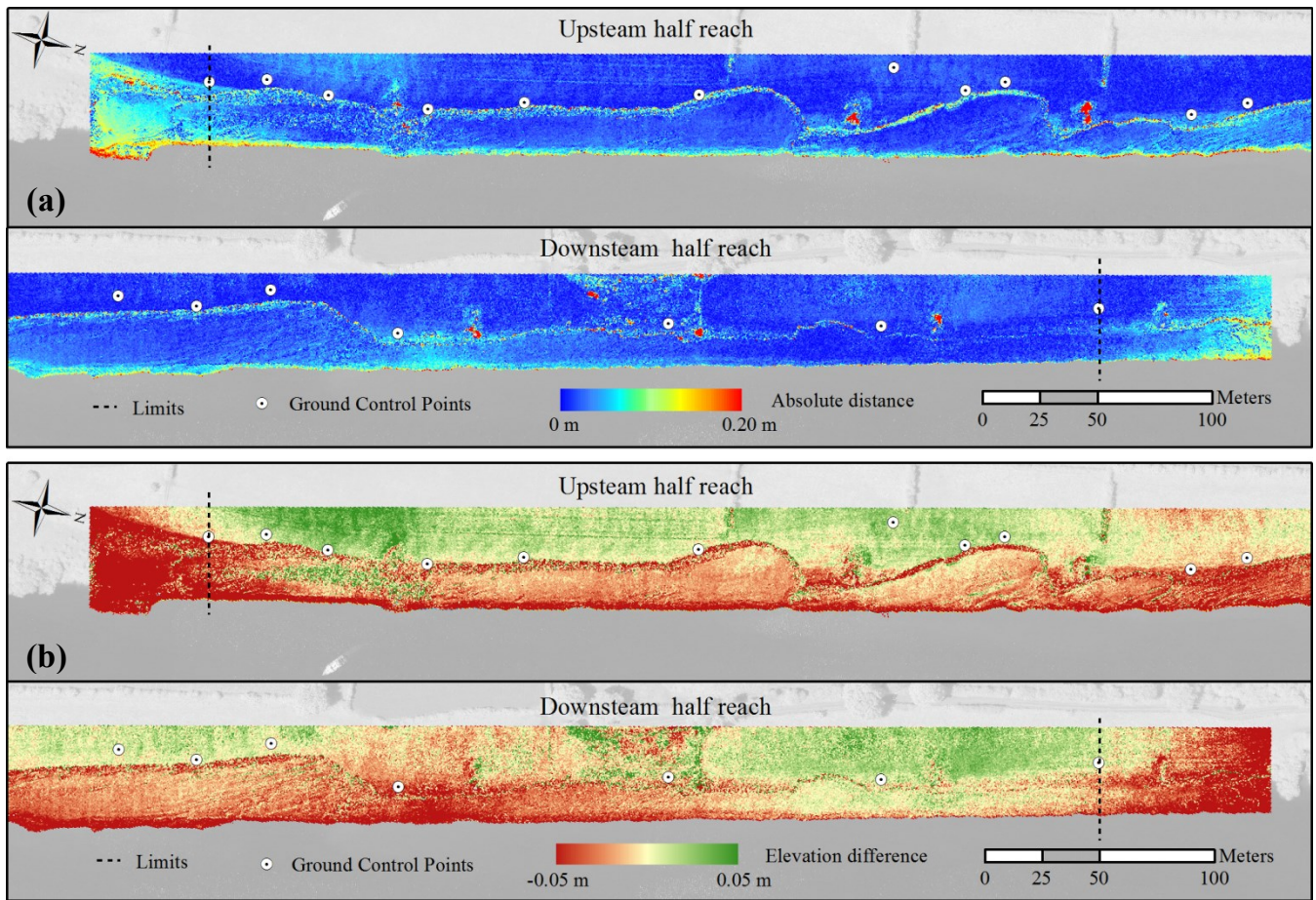
Figure 7: a) Absolute elevation differences between SfM and ALS along the reach. b) Signed elevation differences between SfM and ALS with a smaller scale range.

Figure 7b presents signed elevation differences with a smaller scale range to highlight areas with positive and negative deviations between techniques. Green zones indicate higher ground elevations on the SfM DSM than in the ALS grid, red indicate the opposite, and yellow elevation matches. The upstream half domain presented a general tendency of SfM to overestimate elevations on the floodplain, and in turn underestimate them on the terrace. This trend is also observed in the upper part of the downstream reach. Nevertheless, these zones showed exceptions, such as a green patch at the terrace close to the dashed limit, and a red patch on the floodplain at the end of the upstream half reach. Despite the described general opposed behaviour between floodplain and terrace, the downstream reach evidenced two zones with consistent trends across the domain, covering both the floodplain and terrace. First, lower SfM elevations at the end of the largest embayment (downstream half reach), and second, SfM higher elevations at the end of the reach, before the dashed limit.

Figure 8 presents the relative frequency distributions of the elevation differences divided into three regions: the grassy floodplain, the steep bank, and the bare-ground terrace. Over the grassland, both SfM and ALS had rather similar results (Fig. 8, centre left), with 1 cm mean difference and 2 cm of standard deviation (Table 3). In contrast, the bank had a

bias between techniques of 6 cm (Table 3) and a relatively high standard deviation of the same value. Finally, the terrace showed a slightly higher deviation than over the grassland (Fig. 8 and Table 3) but with a bias of -4 cm. The bank area together with the terrace induce an overall small negative bias in the elevation difference distribution (Fig. 8 left and Table 3). The former with a small contribution to the total number of measurements and the latter with a greater number but a lower magnitude.
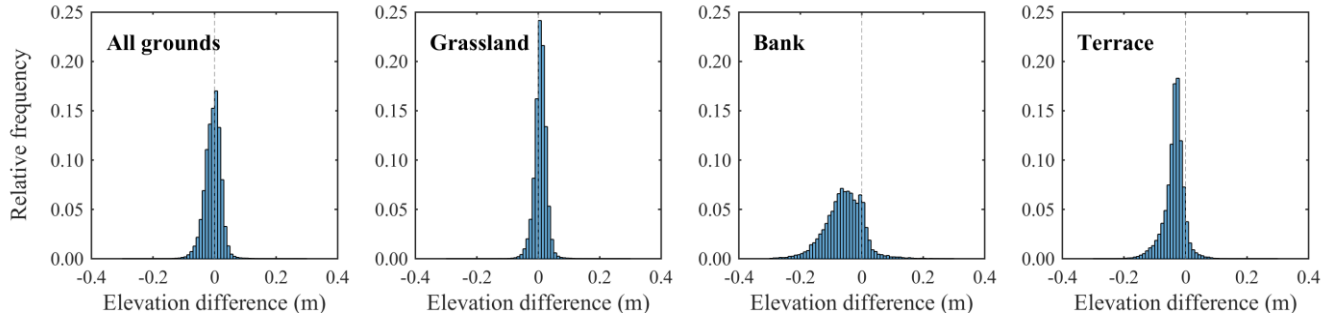
Figure 8: Comparison of elevation differences between SfM and ALS for distinct surface types

Table 3 also indicates the differences of SfM DSM and the ALS with the 129 RTK GPS points. Interestingly, the ALS presented a constant bias of 1 cm across all surfaces, but the standard deviation did change significantly among them: the bank had a standard deviation of 9 cm, which doubled the deviation of the terrace and tripled that of the grassland. While the SFM DSM had comparable absolute biases than those of ALS, the standard deviations were all respectively lower. Particularly at banks, the standard deviation of the SfM DSM was only 3 cm in contrast to the 9 cm of the ALS, which makes the former approach considerably more accurate than the latter. This could explain the relatively large elevation differences between the two methods in the bank area (Fig. 8, centre right), occurring due to a lower precision of the ALS and not vice versa.

Table 3. Mean and standard deviation of elevation differences between SfM, ALS and RTK GPS. Colour intensity indicates the deviation from zero value with minimum/maximum of ±0.09 m.

Subtraction		All grounds	Grassland	Bank	Terrace
SfM - ALS (m)	Mean	-0.01	0.01	-0.06	-0.04
	Std. dev.	0.03	0.02	0.06	0.03
ALS - GPS (m)	Mean	0.01	0.01	0.01	0.01
	Std. dev.	0.05	0.03	0.09	0.05
SfM - GPS (m)	Mean	-0.01	0.01	0.01	-0.02
	Std. dev.	0.03	0.02	0.03	0.02

4.3 DSM accuracy: rotation around GCP axis

A regression line was computed with the locations of the GCPs to analyse with respect to this axis the rotational tendency of the model. The GCP distribution around the regression line and the bankline are shown in Fig. 9 (left). The adopted GCPs spanned 19.7 m across the reach and 1.6 m in the vertical direction (Fig. 9, right). The bank scarp along the reach, which is the target survey area, covered 26.9 m in cross-sectional direction due to the wide-ranging erosion magnitudes of the case study, with maximum bank heights of 3.5 m, indicated with a grey area in the right panel of Fig. 9. This side perspective of the domain evidences the potential plane of rotation, whose stability depends on the position of the GCPs.
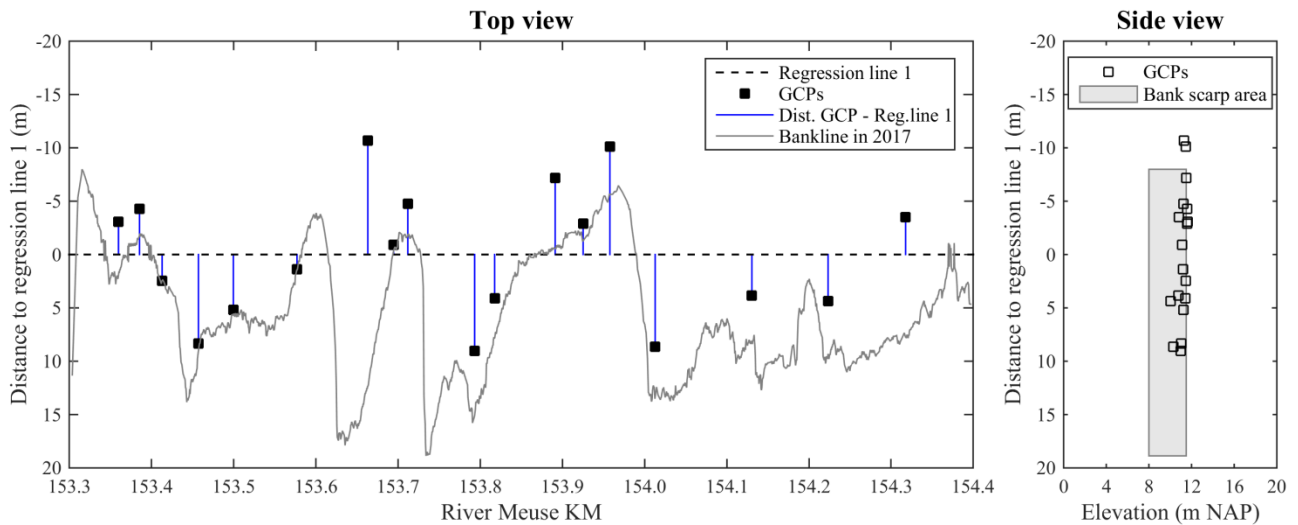
Figure 9: GCP horizontal distances to regression line (left) and respective positions in potential rotation plane from the regression line (right)

The rotation potential of the model is evaluated comparing SfM DSM elevations with those of the 129 GPS points (Fig. 4). Fig. 10a presents the locations of the GPS points used for accuracy control projected at the potential rotation plane, showing that they covered the domain across the channel (abscissa axis) and different elevations along of the scarp area (ordinate axis), resulting in a reasonable sample to assess the model georeferentiation stability. Fig. 10b presents the DSM elevation errors distributed across the regression line 1. In this plane, a second regression line was computed with all 129 points, represented with a dashed black line in Fig. 10b. This line is tilted from the horizontal suggesting that the model was rotated with a magnitude equal to the respective slope.
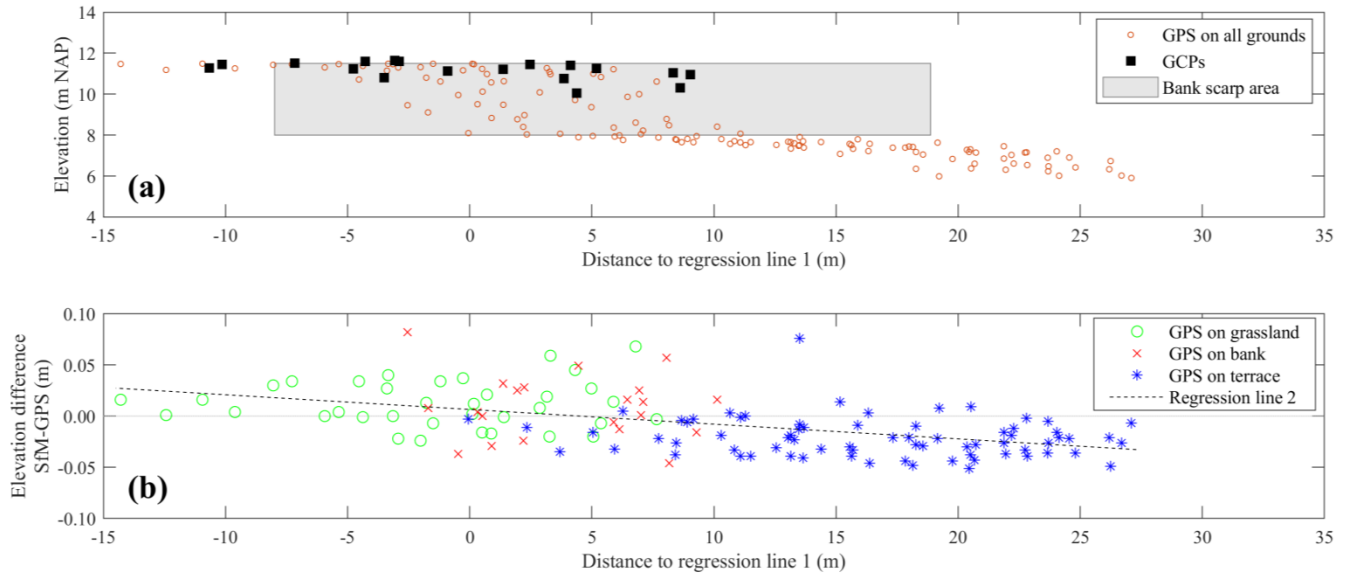
Figure 10: a) Location of GPS measurements in potential rotation plane around regression line 1. b) SfM DSM elevation errors across regression line 1, distinguished among areas of grassland, bank and terrace.

The GPS points corresponded to difference surface types, shown with different point markers in Fig. 10b. It is clear that on the left side to the regression line 2 down-crossing, errors mostly had a positive bias, whereas on the right they mostly presented a negative bias. At the same time, those errors with positive bias were generally over a ground covered with grass, and those with negative trend were measured on a slightly sloped bare ground (see also Table 2, column for Test 3). Then, this tendencies could also be ascribed to the overestimation of the grass cover in the former case, and a non-linear transverse deformation beyond the GCP bounds, for the latter. Regardless of the causes, the results showed an overall transverse DSM inclination with respect of the GPS points used for accuracy control. The regression line 2 when evaluated at the extremes of the bank scarp area (-7.99 m and +18.87 m) yielded an elevation difference between these points of 3.9 cm.

4.4 Bank erosion features and process identification

Six bank profiles were selected among those surveyed with GPS on January 2017 (Fig. 4) to compare the bank representation with the different survey techniques. Fig. 11 shows the bank profiles at sections 1, 2, 4, 6, 7 and 8. These sections presented distinct erosion magnitudes and features after seven years of restoration, for example, section 8 (Fig. 4 and 11) appeared close to the original condition, with a mild slope and nearly no erosion, whereas sections 6 and 7 had vertical scarps. The SfM DSM profiles are represented by continuous lines, the ALS profiles with dashed lines, and GPS points with circles. The SfM representation had better proximity to the GPS points than the ALS in almost all cases. What is

more, ALS generally overestimated the elevation corresponding to the GPS points, which confirms the bias observed in the comparison of bank elevations shown in Fig. 7 and 8.

SfM profiles showed detailed bank features, such as a collapsed upper bank laying at the toe (section 2), an overhang at the bank top (section 1), small-scale roughness on scarps (sections 6 and 7), and slump-block deposits (section 4). These features appeared as simple shapes in the profiles but they were confirmed with field observations. The ALS depicted simpler profiles, smoothed by coarser resolution, which made it difficult to identify characteristic features of the erosion cycle in them. Yet, ALS profiles had enough point spacing to capture gentle bank slopes with reasonable precision (section 8), but for steeper ones (sections 1, 2 and 4) and specially at scarps (sections 6 and 7), this technique provides lower accuracies.
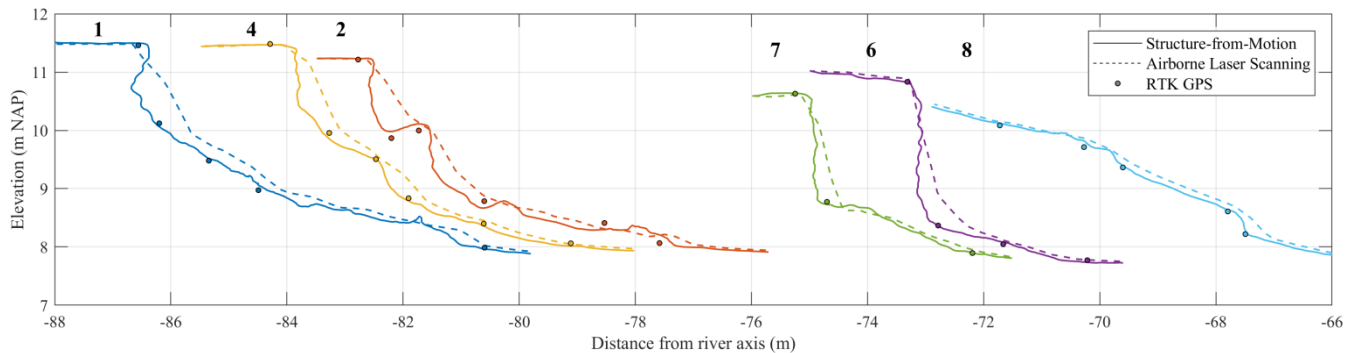
Figure 11: Banks measured with SfM (continuous lines), ALS (dashed lines) and GPS (circles) on 17–18 January 2017. Cross-sections are located from left to right, at river km. 153.4, 153.9, 153.5, 154.2, 154.1, and 154.3 (see Fig. 4 for locations).

The temporal development of section 4 (Fig. 4 and 11) is illustrated in Fig. 12a by a sequence of SfM-UAV surveys. The initial stage corresponds to the survey of Fig. 11 on 18 January 2017. The consecutive surveys showed the evolution of the vertical bank profile, through which different processes can be inferred. The bank profile, initially characterized by a top short scarp and slump blocks along the bank face, experienced a mass failure and a further removal of blocks between January 18 and March 15 2017. Between March 15 and April 26, only toe erosion occurred. By June 21, another mass failure happened, which left slump blocks along the lower half of the bank. On July 19, these blocks were removed, leaving a steep bank face. Then, further toe erosion caused a small soil failure at the lower bank whose remains laid at the toe. On October 11, this wasted material was removed. Then, until the last survey on November 22, entrainment occurred at the lower half of the bank profile, further steepening the bank. In light of the results, the methodology resolution and accuracy are high enough to identify different phases of the erosion cycle, enabling the analysis of bank erosion processes in conjunction with data on potential drivers.
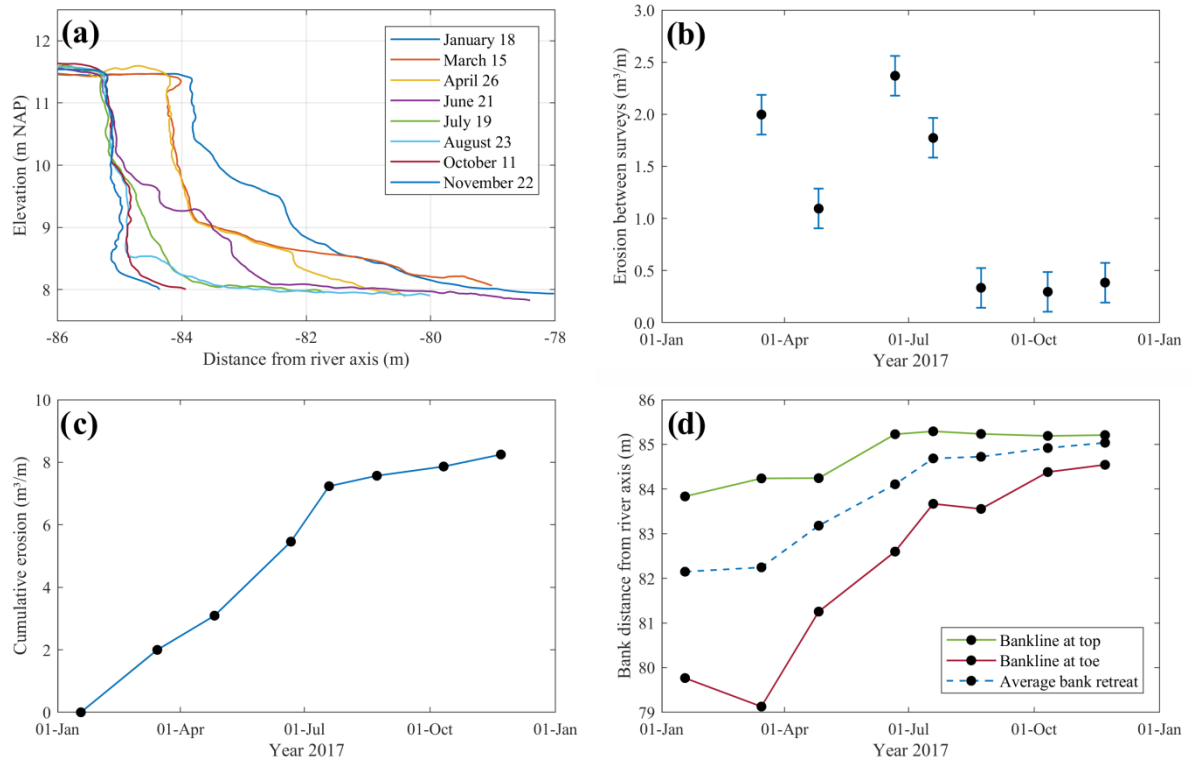
Figure 12: Sequential surveys at cross section 4, Meuse River km. 153.9, over 2017. a) Bank profiles from DSMs; b) Eroded volume per unit width between consecutive surveys; c) Cumulative erosion along surveys; d) Bankline locations at the top and toe of the bank.

In addition to process description, the quantification of eroded volumes is possible computing the net area between sequential bank profiles. For example, Fig. 12b shows eroded volumes per unit width between consecutive surveys plotted at the end of each time interval, with an error bar based on the RMSE of test 3. Evidently, there were different erosion rates during the year and the highest ones happened in the first part of it. Fig. 12c presents the respective cumulative eroded volumes per unit width, where the two trends can be distinguished: a gentle slope towards the end and higher rates of sediment yield during the first haft of the year. Given that the topographic measurements are limited to a single year, it is not possible to state whether this behaviour in recurrent on a yearly basis. However, this case exemplifies the possibilities to quantify eroded volumes throughout different phases of the erosion cycle.

The bankline retreat as a measure of bank erosion involves the identification over time of the bank top, but this concept could be extended, for instance, to the bank toe. Fig. 12d shows the temporal progression of the bankline distance from the river axis for both the bank top and the toe, which we arbitrarily defined for this case at 11.1 m and 8.1 m, respectively. The top bankline showed a mayor jump between April and June and a smaller one between the first two surveys, corresponding to mass failure events. The bank toe presented a more gradual retreat, with events of slumping and temporal accretion that were timely captured along the surveys. This alternative bank retreat representation provides

evidence of the development of bank erosion at every survey. The contrast of bankline retreats at the top and toe of the bank illustrates how different processes on their own represent dissimilar erosion evolutions, since they constitute different phases of the erosion cycle, i.e. at the top mass failures and the toe slump block removal and entrainment. Finally, the average bankline between bank toe and top would best represent the real retreat (dashed line in Fig. 12d), despite not necessarily indicating an actual bank location for a specific elevation. This approach logically considers all erosion phases and follows a similar trend as the cumulative erosion of Fig. 12c.

Figure 13: Zoomed-in UAV photos from track 1 at section 4, km. 153.9, showing diverse bank erosion stages: slump blocks at bank toe on June 21 (left), clean bank face after block removal on July 19 (centre), and undermining on August 23 (right).

Finally, the availability of the UAV imagery provides additional information to analyse and interpret bank evolution through direct observation. Figure 13 shows photographs from the three consecutive surveys on June 21, July 19 and August 23 at section 4, km. 153.9. At this bank area, the sequence shows on the left side of the panels only entrainment at the bank toe, and from the centre (km. 153.9) to the right, one or more erosion cycles. Cross section 4 presented on June 21 (Fig.13, left panel) slump blocks laying at the bank toe that were removed by July 19. Then on August 23, this cross section had incipient undermining at the lower bank and block deposition at the toe. The bank area at the right of section 4 experienced a second mass failure after June 21, completing one erosion cycle, and further downstream it is more difficult to keep track of the cycles due to faster erosion rates. The UAV photos also evidence the progressive growth of grass over the floodplain, especially observable next to the walking path, which was captured along the surveys (Fig. 12a).

5 Discussion

5.1 UAV flight and SfM precision

In general, there were no large differences in accuracy between the DSMs derived with different photo perspectives and overlaps. The precision of the tests, except for test *4*, was approximately 10 cm complying with the target precision and resolution of 14 cm, and they all represented characteristic features of the erosion cycle, such as slump block deposited at the bank toe and mass failures. Other topographic features that were hidden from the nadir UAV perspective, such as undermining, were only captured from oblique camera perspectives. For instance, the area below the top overhangs visible at cross sections 1 and 2 (Fig. 11) were not captured in test *2*, and were represented with a lower resolution in test *4*. The UAV

viewpoint of track 1 not only had the largest bank area coverage compared to the other camera perspectives proposed in this work, but also achieved the highest elevation precision without the need of other tracks. Nevertheless, the nadir view of track 2 contributed to cover an additional bank area behind trees and bushes growing at the bank toe along the first 200 m of the reach (Fig. 2, left), for which it was complementarily used with track 1. Since vegetation can occlude the bank face, if denser

5 and more abundant, it could prevent the usage of the survey technique, in a similar way as high water levels do.

The results herein show that, in the absence of bank toe vegetation, a single oblique UAV track with eight photo overlaps and visible GCPs appears effective to survey banks with the highest precision and coverage, for the given sensor size and resolution, camera-object distance and lighting conditions. This number of photo overlaps agrees with the laboratory experiment of Micheletti et al. (2015), who found that above eight the mean error was only slightly decreased, in contrast to

10 increasing overlaps within the range below eight. Nonetheless, they showed that overlaps higher than eight reduced the number of outliers, a trend which in our case is evident for less overlaps: test *1c* (4 overlaps) mainly differed from test *1b* (8 overlaps) in a higher RMSE but not in the mean. This difference may arise from the distinct texture and complexity of each surface, which presumably requires different number of images for a similar performance (James and Robson, 2012; Westoby et al., 2012; Micheletti et al., 2015).

15 A RMSE of 2.8 cm to measure a riverbank with the photo combination of test *3* results in a relative precision with respect to the average camera-surface distance of 0.0007 or ~1:1400. This relative precision ratio is somewhat higher than ~1:1000 achieved by James and Robson (2012) for steep irregular features at kilometre-scale in a volcanic crater and decametre-scale in a coastal cliff, whereas our precision is somewhat lower than ~1:2000 those authors proved at metre-scale. More precise results could be possible using a bigger and higher-resolution sensor, flying closer to the bank, or even

20 trying other oblique bank perspectives. However, this endeavour would only be reasonable if such data are needed for research purposes and if GCP positioning had also according higher precisions, since registration errors translate into the DSM accuracy during camera parameter optimization (Harwin and Lucieer, 2012; Javernick et al., 2014; Smith et al., 2014).

A precision of 10 cm has implications for the representation of small-scale features at bank scarps. Despite the presence of features in the order of decimetres, we could not assess their accuracy given the discrete GPS points and the

25 0.5 m ALS grid used to assess the DSM precision. For instance, Fig. 12a shows an upper bank scarp along the last four surveys that, if assumed unchanged, it would indicate a maximum distance of 20 cm between surveys, which still would remain within the ±10cm error estimated by the GPS comparison. Although these differences could have been caused by weathering processes or growing grass on the bank face, potential sources of error at such scale could be given, for instance, by registration errors or occlusions caused by the surface roughness (Lague et al., 2013). Then, further research is needed to

30 evaluate the precision at the roughness scale to, for example, analyse form drag at the bank face (Leyland et al., 2015).

The analysis made for test 3 on model rotation evidenced a linear trend with increased surface elevations on the floodplain side of the domain and decreased elevations on the main channel side (Fig. 10b). This tendency was probably caused by a rotation of the DSM around co-linear GCPs that may lead to rotated solutions of the Helmert transformation (Carbonneau and Dietrich, 2017). Yet, the areal SfM-ALS comparison within ± 5 cm range (Fig. 7b), did not evidence a

clear axis along the whole domain that could suggest a rigid rotation of the DSM, since the ALS did have a constant mean accuracy across all surface types (Table 3). The linear rotation tendency, then, might have been obscured by the error range that was larger across the domain (Fig. 6 centre left and 10b) than the mean rotation magnitude, whose elevation difference between the extremes of the cross-sectional domain was 6 cm, and 4 cm within the bank area. Thus, other sources of error

5   were also present that resulted in the obtained error range.

        The comparative analysis of the DSM elevation errors from different photo combinations showed that the ground surfaces surveyed in the case study had different precisions. The grassland presented similar errors with a positive bias throughout all tests. The positive elevation differences are typical of vegetated surfaces (Westoby et al., 2012; Micheletti et al., 2015), whereas the similar performance of different photo combinations might be due to the presence of sufficient and

10   well distributed GCPs in this area (the floodplain). The terrace at the toe of the bank, in contrast, presented different error skewness throughout the tests, which affected the error distribution for all grounds. Interestingly, the error deviation of tests 1 increased as the overlaps decreased, which in turn implies that more overlaps created more robust models. The linear errors cannot explain this behaviour because the same GCP locations were used for all tests, and only the camera parameters were optimized for each.

15   The error skewness at the terrace throughout the tests could be related to the fact that this area was the most distant from the GCPs and it was not surrounded by them, so that errors in lens distortion corrections could have especially increased here (James and Robson, 2014; Javernick et al., 2014; Smith et al., 2014). This effect was clear at the reach extremes (Fig. 7), where the elevation differences increased with respect to the ALS survey further from the GCPs, for which it is called 'dome' effect. While James and Robson (2014) showed that using different (convergent) camera angles is

20   effective to mitigate the 'dome' effect, our results showed that the DSM precision with eight photo overlaps along a single UAV track did not substantially improve by adding the extra perspective of track 2. This may imply that the chosen number of overlaps and used GCPs were sufficient to avoid distortions in the bank area that exceed the required accuracy, together with the fact the track had oblique and not nadiral perspective.

        It is most likely that all the mentioned types of error were present in the SfM DSM, i.e., linear errors given by

25   rotation (linear trend of errors across potential rotation plane, Fig. 10b), non-linear errors given by the estimation of camera parameters (patches of higher or lower SfM elevations across the domain compared to ALS, Fig. 7b), overestimation of ground elevation with grass cover (Table 2, Fig. 7b, Fig 12a), and random errors given by the bundle adjustment that could not be assessed herein. Although, the adopted workflow was effective to measure bank erosion processes with the target accuracy, linear and non-linear errors could have been reduced, for instance, using a larger cross-sectional GCP distribution

30   or better visible and bigger GCP targets. Other possibilities are also open, such as combining two oblique perspectives with a second angle better capturing the floodplain, GCPs and bank area.

5.2 Comparison of two reach-scale techniques: SfM and ALS

The elevation bias at the bank between the SfM-based DSM and the ALS grid (Fig. 8) was caused by the topographic overestimation of ALS (Table 3 and Fig. 9). This ubiquitous error is ascribed to a known limitation of ALS systems related to the laser beam divergence angle, which locates the closest feature within the laser footprint at the centre of the footprint. This increases the ground elevation at high-slope areas (Bailly et al., 2012), which is the case for riverbanks. Still, the ALS resolution and precision were enough to identify bank slopes, in accordance with other studies (e.g., Tarolli et al., 2012; Ortuño et al., 2017). Furthermore, despite the ALS capability to estimate volume changes of eroded banks (Kessler et al., 2013), the method omits information related to the phases of the erosion cycle by not surveying erosion features smaller than its resolution (in this case 0.5 m), apparent in contrast with SfM profiles (Fig. 11). Moreover, if finer ALS resolutions are available, for instance using higher frequency lasers or working with the raw data, more ground details can be captured, but still vertical or undermined profiles would be missed.

The elevation differences between the methods observed for grassland (Fig. 8, centre left) were probably caused by dissimilar ground resolutions, because a larger elevation scatter is expected in the SfM-based DSM when capturing grass with 2 cm resolution, compared to the interpolated ALS samples into a 50 cm grid, even when derived from 0.16 m beam footprints. Nonetheless, the mean difference was zero (Table 3), so that both methods overestimate in the same way the real ground elevation due to grass cover. The effect of this is visible, for instance, in the increasing surface elevations on the floodplain over a year (Fig. 12a), which happens after the mowing period in October. The terrace at the bank toe presented a similar scatter as grassland, but had a small negative bias that could be explained by a DSM rotation or a slight transverse 'dome' effect of the SfM DSM.

The distance covered by the SfM-UAV method depends on the flight autonomy. The deployed UAV had autonomy of approximately 25 minutes, which limited the maximum bank survey extent to approximately 2 km for the tested UAV height and speed, and camera resolution and shutter frequency. This practical limit will change with the progressive development of UAVs, but the distance covered by a single flight is currently significantly smaller than the one covered by ALS. Although a larger camera-object distance and speed than the used in this work would increase the surveyed area, decreasing the ground resolution and the UAV stability may result in the loss of sufficient detail to capture erosion features, and what is more, decrease the DTM precision that depends on the image scale (James and Robson, 2012; Micheletti et al., 2015). Therefore, further investigations would be required to explore the practical limits of UAV-bank monitoring in views of extending the survey coverage.

5.3 UAV-SfM challenges to measure bank erosion processes

The use of UAV-SfM to measure bank erosion processes presents specific challenges, since bank areas usually have vertical surfaces and lengths can be much larger than the other two dimensions. Furthermore, the reach under analysis was particularly straight, introducing additional complexity to apply the technique.

5.3.1 Vertical surfaces

The bank presented steep, vertical and undermined surfaces that required an oblique camera perspective to adequately capture it, whereas GCPs needed sufficient visibility from this angle too. Logically, the visualization and accessibility of GCPs depend on where and how they are placed across the bank profile. In our approach, GCP targets were horizontally placed over the floodplain and close to the bankline, covering 20 m across the channel, which was convenient for a fast field campaign. However, GCPs were not placed at the bank toe or over the bank face so a very limited vertical extent was covered (Fig. 9-10), and the target area was not surrounded by GCPs along the three dimensions. Although a larger vertical range may be effective to reduce potential non-linear errors at the bank, the linear errors may not significantly be reduced with GCP at the toe, given the relatively short bank height (~3.5 m) and corresponding horizontal extent. In our case study, there were no clear non-linear effects at the bank area that could justify the placement of GCPs along the bank face.

The visible dimension of the GCP is proportional to the cosine of the viewing angle with respect to the normal of the plane in which the GCP lies (say α), which increased the uncertainty to locate the target centre along the transverse direction, thus hindering the model georeferentiation when a single UAV track was used. On the other hand, targets were not always distorted in longitudinal direction from oblique angles, i.e., when the camera was near the GCP cross-section, so horizontal errors were not as sensitive along the river axis as they were across the channel. Linear positioning errors in the transverse direction directly affect the accuracy to quantify erosion rates since this is based on the change of bank face positions over time. Moreover, the error introduced by a coarser resolution translated into elevation errors, and these directly affect rotational errors. On the other hand, the lateral view helped to compensate for this, since this elevation errors decreased with the cosine of α.

5.3.2 Linear domain

Banks, considered from the reach scale, are linear domains that extend along the river with the other two dimensions much shorter than their length. The choice of UAV tracks parallel to the river axis simplifies the mission set up and shortens the flying time too. However, this configuration does not provide additional stabilization to the DSM because it is closely aligned with the potential axis of rotation. The adopted approach relied on GCPs to georegister the DSM, which proved effective for the target accuracy. Since parallel UAV tracks tend to increase doming effects (James and Robson, 2014), GCPs were also important to prevent excessive non-linear errors for the required accuracy. Fig. 7b showed no significant DSM deformations within the GCPs, but increasing errors outside the GCP bounds, for which they need to be carefully distributed.

5.3.3 Recommendations

Although the adopted approach attained the required DSM accuracy, further refinement in the workflow could improve the model quality. First, it is advisable to use inclined targets perpendicular to the line of sight of the camera, placing them somewhat parallel to the bank surface, to reduce linear errors as discussed in Sect. 5.3.1. This could be done, for example, with a back stand on rigid plaques. Second, we recommend utilizing two set of GCPs, one set aligned close to the bankline, and another set far away from it. For instance, if the first GCP line is 40 m from the UAV camera in oblique direction (Fig. 3b), the second line could be placed 51 m further inland from the first line to be 80 m from the UAV sensor (twice as far). The latter would need targets four times as big as those next to the bankline to linearly compensate for the decrease in the image resolution (although no linear trend was found between errors and sensor-object distance, Eltner et al., 2016), but these targets in turn could be spaced with double distance while keeping the same number of photo overlaps that capture them. In this example, the rotational error would decrease 2.5 times compared to the results presented here, given by the increase in the cross-sectional GCP footprint and considering similar elevation errors (from GPS and image identification).

In our approach, GCPs were manually identified in the photographs based on three concentric geometries: the inner and outer circles of the CD reflective area and the tile perimeter. The errors introduced during the target identification affect the georeferentiation, and although errors may compensate if not systematically biased, their influence is higher the narrower the cross-sectional GCP span due to the rotation tendency of elongated domains. This source of error can be reduced with wider GCP patterns as suggested above, but also through other improvements, such as automated identification of GCP and Monte Carlo tests (James et al., 2017), to identify more accurately the GCP and optimize the number of GCP and minimize DSM errors.

The camera could be manually set to optimally capture the texture of the bank scarp. In this respect, GCP targets should ideally have a similar reflecting surface to project to the camera a similar amount of light for their later identification. A tilted target would also contribute to have similar reflecting conditions after comparable orientations to the bank with respect to the sun. Furthermore, if the date of the survey campaign is flexible, then overcast but bright days are advisable whenever possible. This is to avoid overexposed or underexposed bank areas due to direct sun light and shades that result in lower image textures within each of these zones and thus in a lower number of detected image features (James and Robson, 2012; Gómez-Gutiérrez et al., 2014a). For example, note in the central photo of Fig. 13 that there were no textural differences due to shades but only due to the bank surface.

5.4 Surveying bank erosion with UAV-SfM and other techniques

Sequential surveys allowed to capture different phases of the erosion cycle (Fig. 12a), which demonstrates that quantitative detection of processes is feasible. Previous studies on bank erosion proved the capabilities of SfM for post-event analysis (Prosdocimi et al., 2015), e.g. representing block deposition, or for 2.5D bank retreat quantification (Hamshaw et al., 2017), whereas herein all erosion phases were sequentially captured, demonstrating the 3D potentialities over the complete process

of erosion. Of course, the ability to monitor banks at the process scale depends on the time interval with which the method can re-survey the exposed part of banks and will only cover pre- and post-flood conditions. The survey frequency and the duration of a full cycle of erosion determine the temporal resolution with which the development of processes is captured. Then, the bank retreat rate of each case determines the necessary frequency of surveys to capture erosion processes within a single cycle. Bank erosion rates naturally depend on each site, after different river sizes, hydraulic conditions, bank materials, etc. In the presented study site erosion rates varied enormously (Fig. 3), but still the performed eight surveys within a year successfully captured bank processes within a single erosion cycle in areas of fast retreat such as section 4.

The study site with a regulated water level and recently restored actively eroding banks was a perfect example for the application of this technique, because banks were exposed and erosion rates were compatible with the proposed average sampling frequency of six weeks. For other types of rivers, where erosion mainly occurs during floods when banks are not exposed, this method would allow measuring pre- and post-event conditions only. Given the high resolution achieved, the method is applicable to all river sizes. However, with the accuracy of the adopted workflow, the application is only advised in cases where bank retreat is larger than approximately 30 cm between consecutive surveys.

Erosion processes happening at small spatial scales, such as weathering, would be hardly or not measurable with the precision achieved in this investigation. For this, other methods are already available, for instance TLS and boat-based laser scanning, that provide higher precisions (mm before registration errors, e.g., O'Neal and Pizzuto, 2011) and comparable resolutions (cm, e.g., Heritage and Hetherington, 2007). In addition, close-range terrestrial photogrammetry can also offer the necessary precision for such endeavours, e.g., from a tripod (Leyland et al., 2015) or a pole on the near-bank area (Bird et al., 2010), at the expense of covering shorter bank lengths. Another alternative are erosion pins, which may also provide higher accuracies, yet with point resolution.

UAV-SfM appears a suitable survey method for both process identification and volume quantification in bank erosion studies, given the decimetre precision range with 3 cm RMSE and the 3D high resolution achieved with a low-cost UAV. As Resop and Hession (2010) suggested, high-resolution three-dimensional capabilities offer great possibilities when spatial variability of retreat is critical compared to traditional cross-profiling methods. In addition, the reduced deployment time of UAVs in the field is advantageous in relation to cross-profiling, while it also improves identification of complex bank features (Fig. 11) and volume computations as other 3D high-resolution techniques (O'Neal and Pizzuto, 2011). Nonetheless, UAV-SfM requires longer post-processing times at the office, which should not be underestimated (Westoby et al., 2012; Passalacqua et al., 2015).

This technique remains less expensive than TLS or MLS, for which it is more convenient for cases where roughness is beyond the scale of interest, and target bank lengths are smaller than 3000 m. This would approximately be the longest distance for a single UAV flight in our case study. For longer reaches, MLS would then compete with UAV-SfM from a practical perspective, since more than one survey/flight would be needed. n all TLS, MLS and UAV-SfM would have limitations to survey the bank surface in presence of dense bank vegetation (Hamshaw et al., 2017). In these cases, ALS provides an alternative, albeit with significant lower resolution and higher costs (Slatton et al., 2007).

For large river extents, i.e., several kilometres, Grove et al. (2013) showed that process inference is possible combining ALS with high-resolution aerial photography, two techniques that are typically applied for eroded volume estimations and bank migration (Khan and Islam, 2003; Lane et al., 2010; De Rose and Basher, 2011; Spiekermann et al., 2017). In that work, the scale of the river (banks higher than 6 m) allowed a spatial resolution of 1 m to capture features that together with photo inspection provided information on mass failure type and fluvial entrainment. To date, UAV-SfM covers smaller extents (Passalacqua et al., 2015), but provides much higher resolutions, allowing for process identification (such as undermining) and more precise volume computations (see Fig. 11 for profile differences between ALS and SfM). For a similar (or higher) accuracy and resolution than those of UAV-SfM and large distances, boat-based laser scanning becomes an attractive, but more expensive, solution.

6 Conclusion

This work evaluated the capability of Structure from Motion photogrammetry applied with low-cost UAV imagery to monitor bank erosion processes along a river reach. The technique's precision was investigated by comparison with GPS points and an airborne laser scanning. Vertical bank profiles were analysed to identify stages of erosion and infer processes. We used a consumer-grade UAV, straight flight paths and a standard SfM workflow that achieved sufficient accuracy and resolution to recognize and quantify the different phases of the bank erosion cycle from bank profiles. Further refinements to the workflow are possible which could reduce linear errors and increase accuracy.

For the adopted approach, the accuracy of the DSM constructed with the SfM technique did not significantly increase with more than eight photo overlaps along a single oblique UAV track. The coverage of bank area behind bank toe vegetation, on the other hand, was increased by adding a vertically oriented perspective, albeit without a significant accuracy increase. As a result, banks were surveyed with 2 cm resolution and a 10 cm elevation precision, whose mean was 1 cm and standard deviation 3 cm (~1:1400 relative to camera-object distance, in line with previous SfM topographic applications). This accuracy was confirmed along the river reach with airborne laser scanning, although the latter overestimated elevations over bank slopes. Higher SfM errors were observed in areas beyond the extent of ground-control points, showing that control points should also be placed outside the monitoring reach and close to the bankline. Furthermore, the GCP distribution across the floodplain proved important to prevent model rotation along GCP axes, so a second line of GCP located further inland is recommended together with proper targets, to reduce model errors as much as possible.

This investigation demonstrates the capabilities of a low-cost UAV to monitor banks at the process scale, while covering a mid-sized river reach of 1.2 km long in a single campaign. The combination of UAV and Structure from Motion photogrammetry can provide relevant information of the spatial structure of bank erosion processes, and with sufficient frequency of acquisition, represent the temporal evolution of morphological processes within the erosion cycle. This method can also be used to compute eroded volumes throughout different phases of the cycle and analyse the contribution of each mechanism to overall retreats. The applied technique is most suitable when measuring bank lengths not exceeding 3000 m,

and its flexibility, fast deployment and high resolution are especially convenient for surveying highly irregular banks. While this method can survey the full cycle of erosion, and not only pre- and post-event conditions, its main limitations are dense riparian vegetation and high water levels, as for most survey techniques.

Data availability

5   The data utilized in this work is publicly available at https://doi.org/10.4121/uuid:4eab4339-52d6-4328-81b2-640544c05438.

Author contribution

The field campaigns, data processing, data analysis and discussion of results were carried out by the first author. The writing of the manuscript was done by the first and second authors. The team authors provided expert opinion, refinement of paper
10 writing and figures, and ideas that improved the final quality of this work.

Acknowledgements

This study was part of the RiverCare research programme, funded by NWO/STW (project number 13516). The research has benefitted from cooperation within the network of the Netherlands Centre for River Studies (NCR). We would like to thank Jaap van Duin and Ruben Kunz for their assistance during the field campaigns. We are grateful to Hans Bakker from
15 Rijkswaterstaat for timely sharing the ALS data.

References

Alho, P., Kukko, A., Hyyppä, H., Kaartinen, H., Hyyppä, J., and Jaakkola, A.: Application of boat-based laser scanning for river survey, Earth Surface Processes and Landforms, 34(13), 1831-1838, doi:10.1002/esp.1879, 2009.

ASCE Task Committee on Hydraulics, Bank Mechanics, and Modeling of River Width Adjustment. River width adjustment.
20 I: Processes and mechanisms, J. Hydraul. Eng. 124 (9), 881–902, doi:10.1061/(ASCE)0733-9429(1998)124:9(881), 1998.

Bailly, J. S., Kinzel, P. J., Allouis, T., Feurer, D., and Le Coarer, Y.: Airborne LiDAR methods applied to riverine environments, Fluvial remote sensing for science and management, 141-161, doi: 10.1002/9781119940791.ch7, 2012.

Bangen, S. G., Wheaton, J. M., Bouwes, N., Bouwes, B., & Jordan, C. (2014). A methodological intercomparison of topographic survey techniques for characterizing wadeable streams and rivers, Geomorphology, 206, 343-361,
25 doi:10.1016/j.geomorph.2013.10.010, 2014.

Barker, R., Dixon, L., and Hooke, J.: Use of terrestrial photogrammetry for monitoring and measuring bank erosion, Earth Surface Processes and Landforms, 22(13), 1217-1227, doi:10.1002/(SICI)1096-9837(199724)22:13<1217::AID-ESP819>3.0.CO;2-U, 1997.

Bird, S., Hogan, D., & Schwab, J.: Photogrammetric monitoring of small streams under a riparian forest canopy, Earth

5   Surface Processes and Landforms, 35(8), 952-970, doi:10.1002/esp.2001, 2010.

Brasington, J., Rumsby, B. T., and McVey, R. A.: Monitoring and modelling morphological change in a braided gravel-bed river using high resolution GPS-based survey, Earth Surface Processes and Landforms, 25(9), 973-990, doi: 10.1002/1096-9837(200008)25:9<973::AID-ESP111>3.0.CO;2-Y, 2000.

Brasington, J., Vericat, D., and Rychkov, I.: Modeling river bed morphology, roughness, and surface sedimentology using

10   high resolution terrestrial laser scanning, Water Resources Research, 48(11), doi:10.1029/2012WR012223, 2012.

Carbonneau, P.E. and Dietrich, J.T.: Cost-effective non-metric photogrammetry from consumer-grade sUAS: implications for direct georeferencing of structure from motion photogrammetry, Earth Surface Processes and Landforms, 42(3), 473-486, doi:10.1002/esp.4012, 2017.

Cavalli, M., Tarolli, P., Marchi, L., and Dalla Fontana, G.: The effectiveness of airborne LiDAR data in the recognition of

15   channel-bed morphology, Catena, 73(3), 249-260, doi:10.1016/j.catena.2007.11.001, 2008.

Charlton, M. E., Large, A. R., and Fuller, I. C.: Application of airborne LiDAR in river environments: the River Coquet, Northumberland, UK, Earth surface processes and landforms, 28(3), 299-306, doi:10.1002/esp.482, 2003.

Clapuyt, F., Vanacker, V. and Van Oost, K.: Reproducibility of UAV-based earth topography reconstructions based on Structure-from-Motion algorithms, Geomorphology, 260, 4-15, doi:10.1016/j.geomorph.2015.05.011, 2016.

20   Clark, L.A. and Wynn, T.M.: Methods for determining streambank critical shear stress and soil erodibility: Implications for erosion rate predictions, Transactions of the ASABE, 50(1), 95-106, doi:10.13031%2F2013.22415, 2007.

Cook, K.L.: An evaluation of the effectiveness of low-cost UAVs and structure from motion for geomorphic change detection, Geomorphology, 278, 195-208, doi:10.1016/j.geomorph.2016.11.009, 2017.

Couper, P. R.: Space and time in river bank erosion research: A review, Area, 36(4), 387-403, doi: 10.1111/j.0004-

25   0894.2004.00239.x, 2004.

Couper, P. R., and Maddock, I. P.: Subaerial river bank erosion processes and their interaction with other bank erosion mechanisms on the River Arrow, Warwickshire, UK, Earth Surface Processes and Landforms, 26(6), 631-646, doi:10.1002/esp.212, 2001.

Couper, P., Stott, T. I. M., and Maddock, I.: Insights into river bank erosion processes derived from analysis of negative

30   erosion-pin recordings: observations from three recent UK studies, Earth Surface Processes and Landforms, 27(1), 59-79, doi: 10.1002/esp.285, 2002.

Darby, S. E., Rinaldi, M., and Dapporto, S.: Coupled simulations of fluvial erosion and mass wasting for cohesive river banks, Journal of Geophysical Research: Earth Surface (2003–2012), 112(F3), doi: 10.1029/2006JF000722, 2007.

De Rose, R. C., and Basher, L. R.: Measurement of river bank and cliff erosion from sequential LIDAR and historical aerial photography, Geomorphology, 126(1), 132-147, doi:10.1016/j.geomorph.2010.10.037, 2011.

Duró, G., Crosato, A., Uijttewaal, W.S.J., Kleinhans, M.G.: Monitoring bank erosion with Unmanned Aerial Vehicle (UAV) during a low-water event, TU Delft, Dataset, doi:10.4121/uuid:4eab4339-52d6-4328-81b2-640544c05438, 2018.

5 Eltner, A., and Schneider, D.: Analysis of different methods for 3D reconstruction of natural surfaces from parallel-axes UAV images, The Photogrammetric Record, 30(151), 279-299, doi:10.1111/phor.12115, 2015.

Eltner, A., Kaiser, A., Castillo, C., Rock, G., Neugirg, F., and Abellán, A.: Image-based surface reconstruction in geomorphometry–merits, limits and developments, Earth Surface Dynamics, 4(2), 359-389, doi:10.5194/esurf-4-359-2016, 2016.

10 Florsheim, J.L., Mount, J.F., and Chin, A.: Bank Erosion as a Desirable Attribute of Rivers, BioScience, 58(6), 519-529, doi:10.1641/B580608, 2008.

Fonstad, M. A., Dietrich, J. T., Courville, B. C., Jensen, J. L., and Carbonneau, P. E.: Topographic structure from motion: a new development in photogrammetric measurement, Earth Surface Processes and Landforms, 38(4), 421-430, doi:10.1002/esp.3366, 2013.

15 Fukuoka, S.: Erosion processes of natural river bank, Proceedings of the 1st International Symposium on Hydraulic Measurement, Beijing, Vol. 223229, 1994.

Girardeau-Montaut, D.: CloudCompare (version 2.9; GPL software), EDF RandD, Telecom ParisTech, available at: http://www.cloudcompare.org/, last access: January 2018.

Gómez-Gutiérrez, Á., de Sanjosé-Blasco, J. J., de Matías-Bejarano, J., and Berenguer-Sempere, F.: Comparing two photo-
20 reconstruction methods to produce high density point clouds and DEMs in the Corral del Veleta Rock Glacier (Sierra Nevada, Spain), Remote Sensing, 6(6), 5407-5427, doi: 10.3390/rs6065407, 2014a.

Gómez-Gutiérrez, Á., Schnabel, S., Berenguer-Sempere, F., Lavado-Contador, F. and Rubio-Delgado, J.: Using 3D photo-reconstruction methods to estimate gully headcut erosion, Catena, 120, 91-101, doi:10.1016/j.catena.2014.04.004, 2014b.

Grove, J. R., Croke J., Thompson, C.: Quantifying different riverbank erosion processes during an extreme flood
25 event, Earth Surface Processes and Landforms, 38(12), 1393-1406, doi:10.1002/esp.3386, 2013.

Hamshaw, S.D., Bryce, T., Rizzo, D.M., O'Neil-Dunne, J., Frolik, J. and Dewoolkar, M.M.: Quantifying streambank movement and topography using unmanned aircraft system photogrammetry with comparison to terrestrial laser scanning, River Research and Applications, 33(8), 1354-1367, doi:10.1002/rra.3183, 2017.

Hartley, R., and Zisserman, A.: Multiple view geometry in computer vision, Cambridge university press, 2003.

30 Harwin, S., and Lucieer, A.: Assessing the accuracy of georeferenced point clouds produced via multi-view stereopsis from unmanned aerial vehicle (UAV) imagery, Remote Sensing, 4(6), 1573-1599, doi:10.3390/rs4061573, 2012.

Henshaw, A. J., Thorne, C. R., and Clifford, N. J.: Identifying causes and controls of river bank erosion in a British upland catchment, Catena, 100, 107-119, doi:10.1016/j.catena.2012.07.015, 2013.

Heritage, G., and Hetherington, D.: Towards a protocol for laser scanning in fluvial geomorphology, Earth Surface Processes and Landforms, 32(1), 66-74, doi:10.1002/esp.1375, 2007.

Hooke, J.M.: An analysis of the processes of river bank erosion, Journal of Hydrology, 42(1-2):39-62, doi:10.1016/0022-1694(79)90005-2, 1979.

5 Immerzeel, W. W., Kraaijenbrink, A., Shea, J. M., Shrestha, A. B., Pellicciotti, F., Bierkens, M. F. P., and De Jong, S. M.: Highresolution monitoring of Himalayan glacier dynamics using unmanned aerial vehicles, Remote Sens. Environ., 150, 93–103, doi:10.1016/j.rse.2014.04.025, 2014.

Jacobson A. et al.: Geometry Processing Toolbox, available at: http://github.com/alecjacobson/gptoolbox, last access: January 2018.

10 James, M. R., and Robson, S.: Straightforward reconstruction of 3D surfaces and topography with a camera: Accuracy and geoscience application, Journal of Geophysical Research: Earth Surface, 117(F3), doi:10.1029/2011JF002289, 2012.

James, M. R., and Robson, S.: Mitigating systematic error in topographic models derived from UAV and ground-based image networks. Earth Surface Processes and Landforms, 39(10), 1413-1420, doi:10.1002/esp.3609, 2014.

James, M.R., Robson, S., d'Oleire-Oltmanns, S. and Niethammer, U.: Optimising UAV topographic surveys processed with

15 structure-from-motion: Ground control quality, quantity and bundle adjustment, Geomorphology, 280, 51-66, doi:10.1016/j.geomorph.2016.11.021, 2017.

Javernick, L., Brasington, J., and Caruso, B.: Modeling the topography of shallow braided rivers using Structure-from-Motion photogrammetry, Geomorphology, 213, 166–182, doi:10.1016/j.geomorph.2014.01.006, 2014.

Khan, N. I., and Islam, A.: Quantification of erosion patterns in the Brahmaputra–Jamuna River using geographical

20 information system and remote sensing techniques, Hydrological Processes, 17(5), 959-966, doi: 10.1002/hyp.1173, 2003.

Kessler, A. C., Gupta, S. C., and Brown, M. K.: Assessment of river bank erosion in Southern Minnesota rivers post European settlement, Geomorphology, 201, 312-322, doi:10.1016/j.geomorph.2013.07.006, 2013.

Kimiaghalam, N., Goharrokhi, M., Clark, S. P., Ahmari, H.: A comprehensive fluvial geomorphology study of riverbank erosion on the Red River in Winnipeg, Manitoba, Canada, Journal of Hydrology, 529, 1488-1498,

25 doi:10.1016/j.jhydrol.2015.08.033, 2015.

Lague, D., Brodu, N., and Leroux, J.: Accurate 3D comparison of complex topography with terrestrial laser scanner: Application to the Rangitikei canyon (NZ), ISPRS Journal of Photogrammetry and Remote Sensing, 82, 10-26, doi:10.1016/j.isprsjprs.2013.04.009, 2013.

Lane, S. N.: The measurement of river channel morphology using digital photogrammetry, The Photogrammetric Record,

30 16(96), 937-961, doi:10.1111/0031-868X.00159, 2000.

Lane, S.N., Widdison, P.E., Thomas, R.E., Ashworth, P.J., Best, J.L., Lunt, I.A., Sambrook Smith, G.H. and Simpson, C.J.: Quantification of braided river channel change using archival digital image analysis, Earth Surface Processes and Landforms, 35(8), 971-985, doi:10.1002/esp.2015, 2010.

Lawler, D. M.: Process dominance in bank erosion systems, Lowland floodplain rivers: Geomorphological perspectives, 117-43, 1992.

Lawler, D.M.: The measurement of river bank erosion and lateral channel change: a review, Earth surface processes and landforms, 18(9), 777-821, doi:10.1002/esp.3290180905, 1993.

5   Lawler, D.M.: The importance of high-resolution monitoring in erosion and deposition dynamics studies: examples from estuarine and fluvial systems, Geomorphology, 64(1), 1-23, doi:10.1016/j.geomorph.2004.04.005, 2005.

Leyland, J., Darby, S. E., Teruggi, L., Rinaldi, M., and Ostuni, D.: A self-limiting bank erosion mechanism? inferring temporal variations in bank form and skin drag from high resolution topographic data, Earth Surf. Process. Landforms, 40: 1600–1615, doi:10.1002/esp.3739, 2015.

10   Massey, D.: Talking of space-time, Transactions of the Institute of British Geographers, 26: 257–261, doi:10.1111/1475-5661.00019, 2001.

Micheletti, N., Chandler, J. H., and Lane, S. N.: Investigating the geomorphological potential of freely available and accessible structure-from-motion photogrammetry using a smartphone, Earth Surface Processes and Landforms, 40(4), 473-486, doi:10.1002/esp.3648, 2015.

15   Nardi, L., Campo, L., and Rinaldi, M.: Quantification of riverbank erosion and application in risk analysis, Nat Hazards, 69(1), 869-887, doi:10.1007/s11069-013-0741-8, 2013.

O'neal, M. A., and Pizzuto, J. E.: The rates and spatial patterns of annual riverbank erosion revealed through terrestrial laser-scanner surveys of the South River, Virginia, Earth Surface Processes and Landforms, 36(5), 695-701, doi:10.1002/esp.2098, 2011.

20   Ortuño, M., Guinau, M., Calvet, J., Furdada, G., Bordonau, J., Ruiz, A., and Camafort, M.: Potential of airborne LiDAR data analysis to detect subtle landforms of slope failure: Portainé, Central Pyrenees, Geomorphology, 295, 364-382, doi:10.1016/j.geomorph.2017.07.015, 2017.

Ouédraogo, M. M., Degré, A., Debouche, C., and Lisein,J.: The evaluation of unmanned aerial system-based photogrammetry and terrestrial laser scanning to generate DEMs of agricultural watersheds, Geomorphology, 214, 339–355,
25   doi:10.1016/j.geomorph.2014.02.016, 2014.

Parker, G., Shimizu, Y., Wilkerson, G. V., Eke, E. C., Abad, J. D., Lauer, J. W., Paola, C., Dietrich, W. E., Voller, V. R.: A new framework for modeling the migration of meandering rivers, Earth Surface Processes and Landforms, 36(1), 70-86, doi:10.1002/esp.2113, 2011.

Passalacqua, P., Belmont, P., Staley, D.M., Simley, J.D., Arrowsmith, J.R., Bode, C.A., Crosby, C., DeLong, S.B., Glenn,
30   N.F., Kelly, S.A. and Lague, D.: Analyzing high resolution topography for advancing the understanding of mass and energy transfer through landscapes: A review, Earth-Science Reviews, 148, 174-193, doi:10.1016/j.earscirev.2015.05.012, 2015.

Pyle, C. J., Richards, K. S., and Chandler, J. H.: Digital photogrammetric monitoring of river bank erosion, The Photogrammetric Record, 15(89), 753-764, doi:10.1111/0031-868X.00083, 1997.

Prosdocimi, M., Calligaro, S., Sofia, G., Dalla Fontana, G., and Tarolli, P.: Bank erosion in agricultural drainage networks: new challenges from structure-from-motion photogrammetry for post-event analysis, Earth Surface Processes and Landforms, 40(14), 1891-1906, doi:10.1002/esp.3767, 2015.

Reneau, S.L., Drakos, P.G., Katzman, D., Malmon, D.V., McDonald, E.V., Ryti, R.T.: Geomorphic controls on contaminant distribution along an ephemeral stream. Earth Surface Processes and Landforms, 29(10):1209-23, DOI: 10.1002/esp.108, 2004.

Resop, J. P., and Hession, W. C.: Terrestrial laser scanning for monitoring streambank retreat: Comparison with traditional surveying techniques, Journal of Hydraulic Engineering, 136(10), 794-798, doi:10.1061/(ASCE)HY.1943-7900.0000233, 2010.

Rhoades, E. L., O'Neal, M. A., and Pizzuto, J. E.: Quantifying bank erosion on the South River from 1937 to 2005, and its importance in assessing Hg contamination, Applied Geography, 29(1), 125-134, doi:10.1016/j.apgeog.2008.08.005, 2009.

Rinaldi, M., and Darby, S. E.: Modelling river-bank-erosion processes and mass failure mechanisms: progress towards fully coupled simulations, Developments in Earth Surface Processes, 11, 213-239. doi:10.1016/S0928-2025(07)11126-3, 2008.

Rinaldi, M., Casagli N., Dapporto S., and Gargini, A.: Monitoring and modeling of pore water pressure changes and riverbank stability during flow events, Earth Surf. Processes Landforms, 29, 237–254, doi: 10.1002/esp.1042, 2004.

Siviglia, A., & Crosato, A.: Numerical modelling of river morphodynamics: Latest developments and remaining challenges. Advances in Water Resources, 93(A), 1-3, doi:10.1016/j.advwatres.2016.01.005, 2016.

Slatton, K. C., Carter W. E., Shrestha R. L., and Dietrich W.: Airborne Laser Swath Mapping: Achieving the resolution and accuracy required for geosurficial research, Geophys. Res. Lett., 34, L23S10, doi:10.1029/2007GL031939, 2007.

Stöcker, C., Eltner, A., and Karrasch, P.: Measuring gullies by synergetic application of UAV and close range photogrammetry – A case study from Andalusia, Spain, Catena, 132, 1–11, doi:10.1016/j.catena.2015.04.004, 2015.

Smith, M. W., Carrivick, J. L., Hooke, J., and Kirkby, M. J.: Reconstructing flash flood magnitudes using "Structure-from-Motion": A rapid assessment tool, J. Hydrol., 519, 1914–1927, doi:10.1016/j.jhydrol.2014.09.078, 2014.

Snavely, N., Seitz, S. M., and Szeliski, R.: Modeling the world from internet photo collections, International Journal of Computer Vision, 80(2), 189-210, doi:10.1007/s11263-007-0107-3, 2008.

Spiekermann, R., Betts, H., Dymond, J., and Basher, L.: Volumetric measurement of river bank erosion from sequential historical aerial photography, Geomorphology, 296, 193-208, doi:10.1016/j.geomorph.2017.08.047, 2017.

Tamminga, A. D., Brett C. E., and Hugenholtz C. H.: UAS-based remote sensing of fluvial change following an extreme flood event, Earth Surface Processes and Landforms 40, no. 11, 1464-1476, doi: 10.1002/esp.3728 , 2015.

Tarolli, P., Sofi,a G., Dalla Fontana, G.: Geomorphic features extraction from high-resolution topography: landslide crowns and bank erosion, Natural Hazards, 61(1), 65-83, doi:10.1007/s11069-010-9695-2, 2012.

Telling, J., Lyda, A., Hartzell, P., and Glennie, C.: Review of earth science research using terrestrial laser scanning, Earth-Science Reviews, 169, 35-68, 10.1016/j.earscirev.2017.04.007, 2017.

Thoma, D. P., Gupta, S. C., Bauer, M. E., and Kirchoff, C. E.: Airborne laser scanning for riverbank erosion assessment, Remote sensing of Environment, 95(4), 493-501, doi:10.1016/j.rse.2005.01.012, 2005.

Thorne, C. R.: Processes and mechanisms of river bank erosion, Gravel-bed rivers, 227-259, 1982.

Thorne, C.R. and Tovey N.K.: Stability of composite river banks, Earth Surface Processes and Landforms, 6(5), 469-484, doi:10.1002/esp.3290060507, 1981.

Tonkin, T. N., Midgley, N. G., Graham, D. J., and Labadz, J. C.: The potential of small unmanned aircraft systems and structure-frommotion for topographic surveys: A test of emerging integrated approaches at Cwm Idwal, North Wales, Geomorphology, 226, 35–43, doi:10.1016/j.geomorph.2014.07.021, 2014.

Turner, D., Lucieer, A., and de Jong, S.: Time Series Analysis of Landslide Dynamics Using an Unmanned Aerial Vehicle (UAV), Remote Sensing, 7, 1736–1757, doi:10.3390/rs70201736, 2015.

Westoby, M. J., Brasington, J., Glasser, N. F., Hambrey, M. J., and Reynolds, J. M.: 'Structure-from-Motion' photogrammetry: A low-cost, effective tool for geoscience applications, Geomorphology, 179, 300-314, doi:10.1016/j.geomorph.2012.08.021, 2012.

Woodget, A. S., Carbonneau, P. E., Visser, F., and Maddock, I. P.: Quantifying submerged fluvial topography using hyperspatial resolution UAS imagery and structure from motion photogrammetry, Earth Surf. Proc. Land., 40, 47–64, doi:10.1002/esp.3613, 2015.

Table 1. Number of photographs and overlaps for the tests

	Test 1a	Test 1b	Test 1c	Test 1d	Test 2	Test 3	Test 4	Test 5
Track 1	293	147	73	37		147		293
Track 2					232	232		232
Track 3							232	232
Track 4							232	232
Min. overlaps	16	8	4	2	7	15	26	49
Max. overlaps	20	10	5	2	7	17	26	53

Table 2. Mean and standard deviation of elevation differences between SfM DSMs and GPS points. Colour intensity indicates the deviation from zero value with minimum/maximum of ±0.13 m.

Surface	Error (m)	Test 1a	Test 1b	Test 1c	Test 1d	Test 2	Test 3	Test 4	Test 5
All grounds	Mean	-0.01	0.00	0.00	0.04	0.03	-0.01	-0.05	0.00
	Std. dev.	0.03	0.03	0.04	0.07	0.03	0.03	0.05	0.03
Grassland	Mean	0.02	0.01	0.01	0.02	0.02	0.01	0.01	0.02
	Std. dev.	0.03	0.03	0.04	0.04	0.03	0.02	0.02	0.02
Bank	Mean	0.00	0.01	-0.01	-0.01	0.05	0.01	-0.03	0.01
	Std. dev.	0.04	0.03	0.07	0.13	0.03	0.03	0.04	0.03
Terrace	Mean	-0.02	-0.02	0.00	0.06	0.03	-0.02	-0.09	-0.01
	Std. dev.	0.02	0.03	0.03	0.06	0.03	0.02	0.03	0.02

Table 3. Mean and standard deviation of elevation differences between SfM, ALS and RTK GPS. Colour intensity indicates the deviation from zero value with minimum/maximum of ±0.09 m.

Subtraction		All grounds	Grassland	Bank	Terrace
SfM - ALS (m)	Mean	-0.01	0.01	-0.06	-0.04
	Std. dev.	0.03	0.02	0.06	0.03
ALS - GPS (m)	Mean	0.01	0.01	0.01	0.01
	Std. dev.	0.05	0.03	0.09	0.05
SfM - GPS (m)	Mean	-0.01	0.01	0.01	-0.02
	Std. dev.	0.03	0.02	0.03	0.02